

Searching for Highly Magnified Stars at Cosmological Distances: Discovery of a Redshift 0.94 Blue Supergiant in Archival Images of the Galaxy Cluster MACS J0416.1-2403

Wenlei Chen¹, Patrick L. Kelly¹, Jose M. Diego², Masamune Oguri^{3,4,5}, Liliya L. R. Williams¹, Adi Zitrin⁶, Tommaso L. Treu⁷, Nathan Smith⁸, Thomas J. Broadhurst^{9,10,11}, Nick Kaiser¹², Ryan J. Foley¹³, Alexei V. Filippenko^{14,15}, Laura Salo¹⁶, Jens Hjorth¹⁷, and Jonatan Selsing ^{18,19}

School of Physics and Astronomy, University of Minnesota, 116 Church Street SE, Minneapolis, MN 55455, USA; chen6339@umn.edu

² IF₂CA, Instituto de Física de Cantabria (UC-CSIC), Av. de Los Castros s/n, E-39005 Santander, Spain ³ Department of Physics, University of Tokyo, 7-3-1 Hongo, Bunkyo-ku, Tokyo 113-0033, Japan 4 Research Center for the Early Universe, University of Tokyo, 7-3-1 Hongo, Bunkyo-ku, Tokyo 113-0033, Japan

5 Kavli Institute for the Physics and Mathematics of the Universe (Kavli IPMU, WPI), University of Tokyo, 5-1-5 Kashiwanoha, Kashiwa, Chiba 277-8583, Japan

6 Physics Deposits and Mathematics of the University of the Nearly P.O. Roy 653, Rest-Sheya 8410501, Igrael Physics Department, Ben-Gurion University of the Negev, P.O. Box 653, Beer-Sheva 8410501, Israel Department of Physics and Astronomy, University of California, Los Angeles, CA 90095, USA Department of Astronomy, University of Arizona, Tucson, AZ 85721, USA Department of Theoretical Physics, University of the Basque Country UPV/EHU, E-48080 Bilbao, Spain Donostia International Physics Center (DIPC), E-20018 Donostia, Spain Ikerbasque, Basque Foundation for Science, E-48011 Bilbao, Spain 12 Département de Physique, École Normale Supérieure, Paris, France 13 Department of Astronomy and Astrophysics, University of California, Santa Cruz, CA 95064, USA Department of Astronomy, University of California, Berkeley, CA 94720-3411, USA 15 Miller Senior Fellow, Miller Institute for Basic Research in Science, University of California, Berkeley, CA 94720, USA ⁶ Department of Physics, Hillsdale College, 33 E. College Street, Hillsdale, MI 49242, USA ¹⁷ DARK, Niels Bohr Institute, University of Copenhagen, Lyngbyvej 2, DK-2100 Copenhagen, Denmark ¹⁸ The Cosmic Dawn Center (DAWN), Niels Bohr Institute, University of Copenhagen, Lyngbyvej 2, DK-2100 Copenhagen Ø, Denmark DTU-Space, Technical University of Denmark, Elektrovej 327, DK-2800 Kongens Lyngby, Denmark Received 2019 February 14; revised 2019 June 2; accepted 2019 June 11; published 2019 August 6

Abstract

Individual highly magnified stars have been recently discovered at lookback times of more than half the age of the universe, in lensed galaxies that straddle the critical curves of massive galaxy clusters. Having established their detectability, it is now important to carry out systematic searches for them in order to establish their frequency, and in turn learn about the statistical properties of high-redshift stars and of the granularity of matter in the foreground deflector. Here we report the discovery of a highly magnified star at redshift z = 0.94 in a strongly lensed arc behind a Hubble Frontier Field (HFF) galaxy cluster, MACS J0416.1-2403, discovered as part of a systematic archival search. The bright transient (dubbed "Warhol") was discovered in Hubble Space Telescope data taken on 2014 September 15 and 16. The point source faded over a period of two weeks, and observations taken on 2014 September 1 show that the duration of the microlensing event was at most four weeks in total. The magnified stellar image that exhibited the microlensing peak may also exhibit slow changes over a period of years at a level consistent with that expected for microlensing by the stars responsible for the intracluster light of the cluster. Optical and infrared observations taken near peak brightness can be fit by a stellar spectrum with moderate hostgalaxy extinction. A blue supergiant matches the measured spectral energy distribution near peak, implying a temporary magnification of at least several thousand. The short timescale of the event and the estimated effective temperature indicate that the lensed source is an extremely magnified star. Finally, we detect the expected counterimage of the background lensed star at an offset by ~ 0.11 in a deep coaddition of HFF imaging.

Key words: galaxies: clusters: general – galaxies: clusters: individual: MACS J0416.1-2403 – gravitational lensing: strong – stars: massive

1. Introduction

In 2016 May, imaging of a *Hubble* Frontier Field (HFF) galaxy-cluster field, MACS J1149.5+2223 (MACS1149; redshift z=0.54), revealed a several-week-long transient (F125W (J) ≈ 25.7 mag AB; $i\approx 26.4$ mag AB at peak) in a magnified galaxy at z=1.49 (Kelly et al. 2018). A highly magnified image of the lensed star has always been detected in deep *Hubble Space Telescope* (*HST*) observations, and the spectral energy distribution (SED) of the star measured in HFF imaging in 2014 matches that of the bright transient detected in 2016 May, consistent with temporarily increased magnification. The SED also exhibits a strong Balmer jump present in some luminous stars yet absent from stellar outbursts. Finally, simulations of microlensing of a background star by stars or

remnants in the foreground cluster can produce light curves similar to that observed (Venumadhav et al. 2017; Diego et al. 2018; Kelly et al. 2018). The discovery of the star realized a theoretical prediction that individual stars at cosmological distances could become sufficiently magnified to be detected (Miralda-Escude 1991).

In 2014 January and August, the FrontierSN project (PI: S. Rodney) detected a pair of transients dubbed the "Spock" events at two separate locations in a highly magnified galaxy at z = 1.01 behind the MACS J0416.1-2403 (MACS0416; Ebeling et al. 2001) galaxy cluster (z = 0.397) using *HST*. These events, whose locations are shown in Figure 1, were identified during two month-long campaigns to image MACS0416 as part of the HFF project (PI: J. Lotz). While the events each lasted only

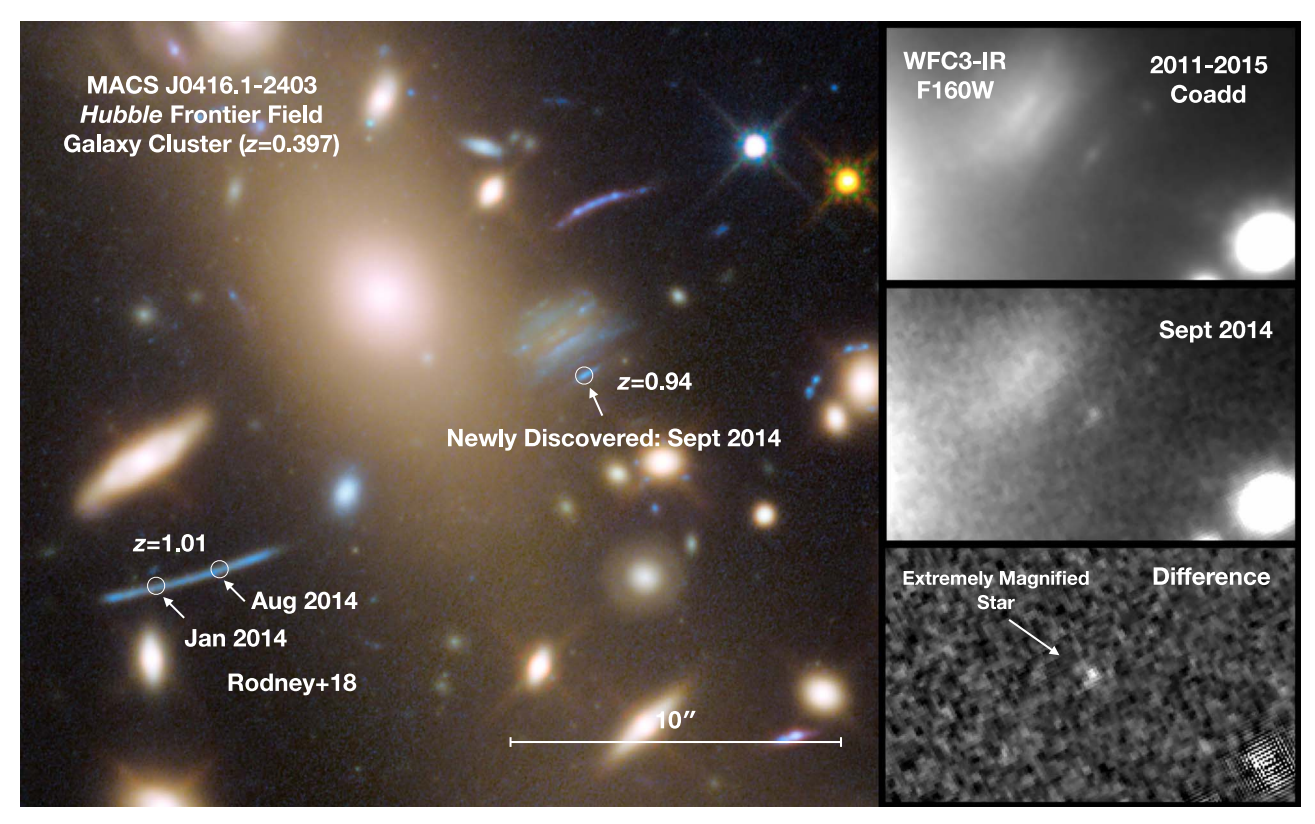


Figure 1. Left panel shows the location of the newly discovered extremely magnified star in an arc at z = 0.94 found in archival *HST* imaging of the MACS0416 galaxy cluster, and the positions of the two stellar microlensing events previously identified by Rodney et al. (2018) in a different strongly lensed galaxy at z = 1.01. The timescales of all three events were several weeks. Right panel shows an example deep template WFC3-IR F160W image of the field (top), image of the newly identified event near peak in 2014 September (middle), and the difference image (bottom).

several weeks, their interpretation was not immediately apparent. The detection of the lensed star in MACS J1149 magnified by >2000 at peak brightness prompted the interpretation of the two MACS0416 events as likely microlensing events (Rodney et al. 2018).

We are conducting a systematic search for transients in the full set of archival *HST* imaging data of HFF galaxy-cluster fields (Lotz et al. 2017). Microlensing fluctuations present in the light curve of a highly magnified star can place unique constraints on the initial mass function and the initial—final mass function of intracluster stars, and on the abundance of primordial black holes (Dai et al. 2018; Diego et al. 2018; Kelly et al. 2018; Oguri et al. 2018). A sample of multiple, highly magnified stars can mitigate the effect of uncertainties in cluster models and improve the strength of constraints on the abundance of primordial black holes. Furthermore, observations of such stars offer the opportunity to study directly the luminous stellar population at high redshifts, which may differ from that in the nearby universe (e.g., Steidel et al. 2014; Sanders et al. 2016).

As shown in Figure 1, we have now identified, in archival HST imaging taken in 2014 September, a third highly magnified star at z=0.94 in the MACS0416 field in a lensed galaxy different from that where the Spocks were discovered. We have named this transient "Warhol" given its "fifteen minutes of fame." Figure 2 shows that the transient is within a small fraction of an arcsecond from the location of the MACS0416 cluster's critical curve according to published models. At these small separations from the critical curve, microlensing of bright stars in a background arc by objects in the foreground cluster including stars or remnants is not only possible, but in fact inevitable.

In Section 2, we describe the imaging data in this paper. Section 3 provides the details of the methods we use to analyze the *HST* imaging. In Section 4, the results of our analysis are presented, and our conclusions are given in Section 5. All magnitudes are in the AB system (Oke & Gunn 1983), and we use a standard set of cosmological parameters ($\Omega_m = 0.3$, $\Omega_{\Lambda} = 0.7$, $H_0 = 70$ km s⁻¹ Mpc⁻¹).

2. Data

Imaging of the MACS0416 galaxy-cluster field with the ACS and WFC3 cameras has been acquired as part of the Cluster Lensing and Supernova survey with Hubble (CLASH; GO-12459; Postman et al. 2012), the Grism Lens-Amplified Survey from Space (PI: T. Treu; GO-13459; Schmidt et al. 2014; Treu et al. 2015), the HFF (GO-13496; Lotz et al. 2017), the FrontierSN follow-up program (PI: S. Rodney; GO-13386), and the Final UV Frontier project (PI: B. Siana; GO-14209). Earlier imaging of the MACS0416 field, not analyzed in this paper, was acquired with the WFPC2 (PI: H. Ebeling; GO-11103). The microlensing peak we report here occurred in the target-of-opportunity imaging follow-up of the Spock events (Rodney et al. 2018) acquired by the FrontierSN program.

3. Methods

3.1. Image Processing and Coaddition

We aligned all imaging with TweakReg, and then resampled images to a scale of $0\rlap.{''}03$ pixel $^{-1}$ using Astro-Drizzle (Fruchter et al. 2010).

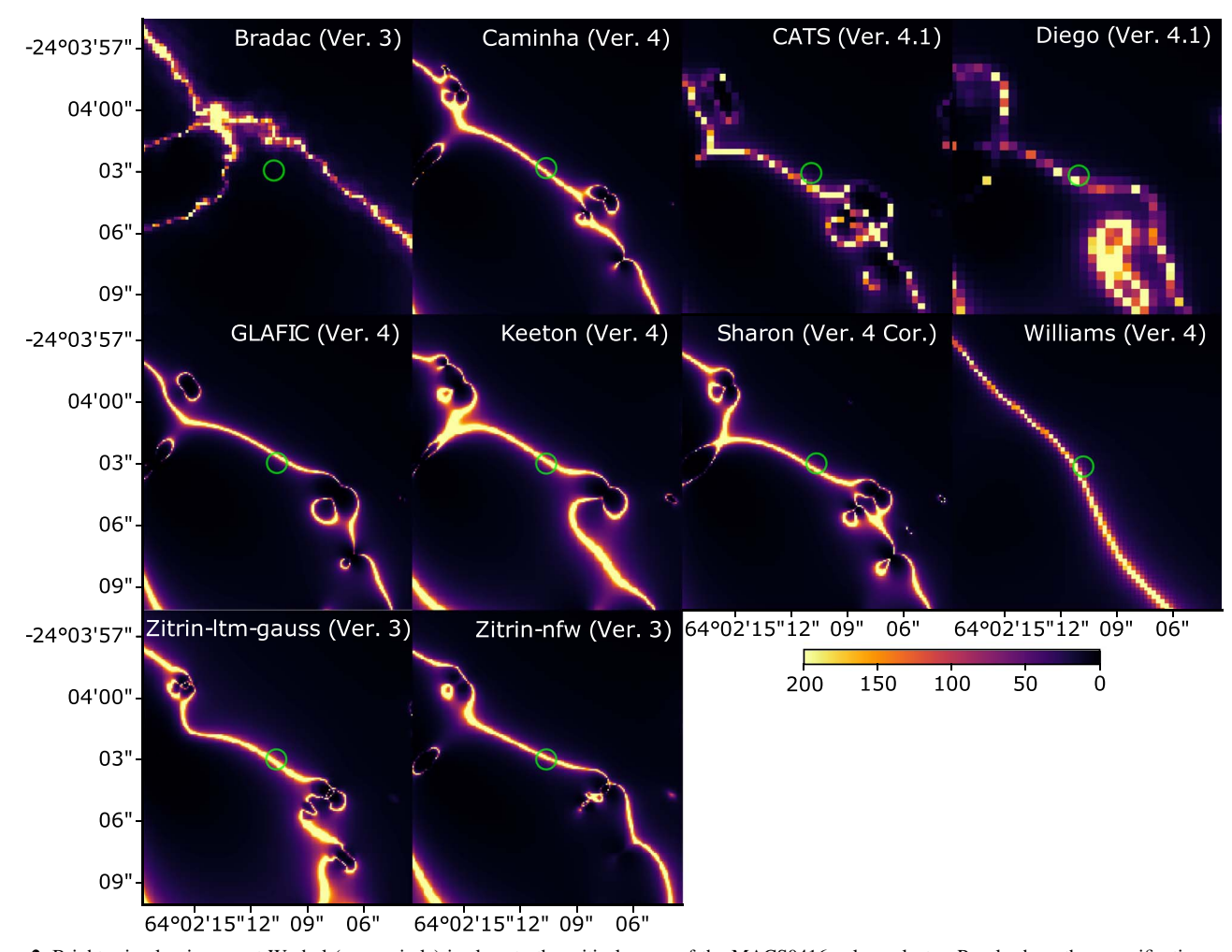


Figure 2. Bright microlensing event Warhol (green circle) is close to the critical curve of the MACS0416 galaxy cluster. Panels show the magnification maps for published lens models (see Table 3 for magnification values). The galaxy-cluster critical curve has a simple configuration close to the location of the microlensing event.

3.2. PythonPhot Photometry

We use PythonPhot²⁰ (Jones et al. 2015) to measure the light curves from difference imaging. The PythonPhot package includes an implementation of point-spread function (PSF) fitting photometry based on the DAOPHOT algorithm (Stetson 1987).

3.3. Transient Detection

For each HST visit, we created a difference image by subtracting a deep template image from a coaddition of exposures acquired during the visit. We next identified all peaks having $>2\sigma$ significance, where σ corresponds to the standard deviation of the background in the difference image. Then we measured the angular size of each of the candidate transients, and we selected objects with an extent consistent with the size of the PSF.

We retained only the peaks that we detected with $> 2\sigma$ significance in multiple *HST* visits at the same location within a 10-day interval, a characteristic timescale for microlensing peaks of magnified stars. Our objective was to identify transients that might have been missed by searches that only scanned images acquired during individual epochs.

4. Results

Warhol is the first highly magnified star that our ongoing archival search program has found that was not already identified.

4.1. Position and Underlying Arc

The transient's J2000 coordinates are $\alpha=4^{\rm h}16^{\rm m}08\,^{\rm s}.7084$, $\delta=-24^{\circ}04'02.''945$ in the World Coordinate System of the official HFF coadded images. A spectrum of the underlying arc acquired by the CLASH-Very Large Telescope survey yielded z=0.93910 (Balestra et al. 2016; Caminha et al. 2017), which is a smaller redshift than those of Icarus (Kelly et al. 2018) and the Spocks (Rodney et al. 2018). Patrício et al. (2018) measure an oxygen abundance of $12+\log({\rm O/H})=8.72\pm0.6$ dex and a low extinction of $A_V=0.15\pm0.20$ from nebular emission lines for the lensed system from Multi Unit Spectroscopic Explorer integral-field unit spectroscopy.

4.2. Light Curve and Duration of Event

The optical and near-infrared light curve plotted in Figure 3 shows that the microlensing event faded over a period of at least two weeks. The event was at least ~ 1.5 times brighter (total flux) in the infrared (IR) band than its underlying arc in

²⁰ https://github.com/djones1040/PythonPhot

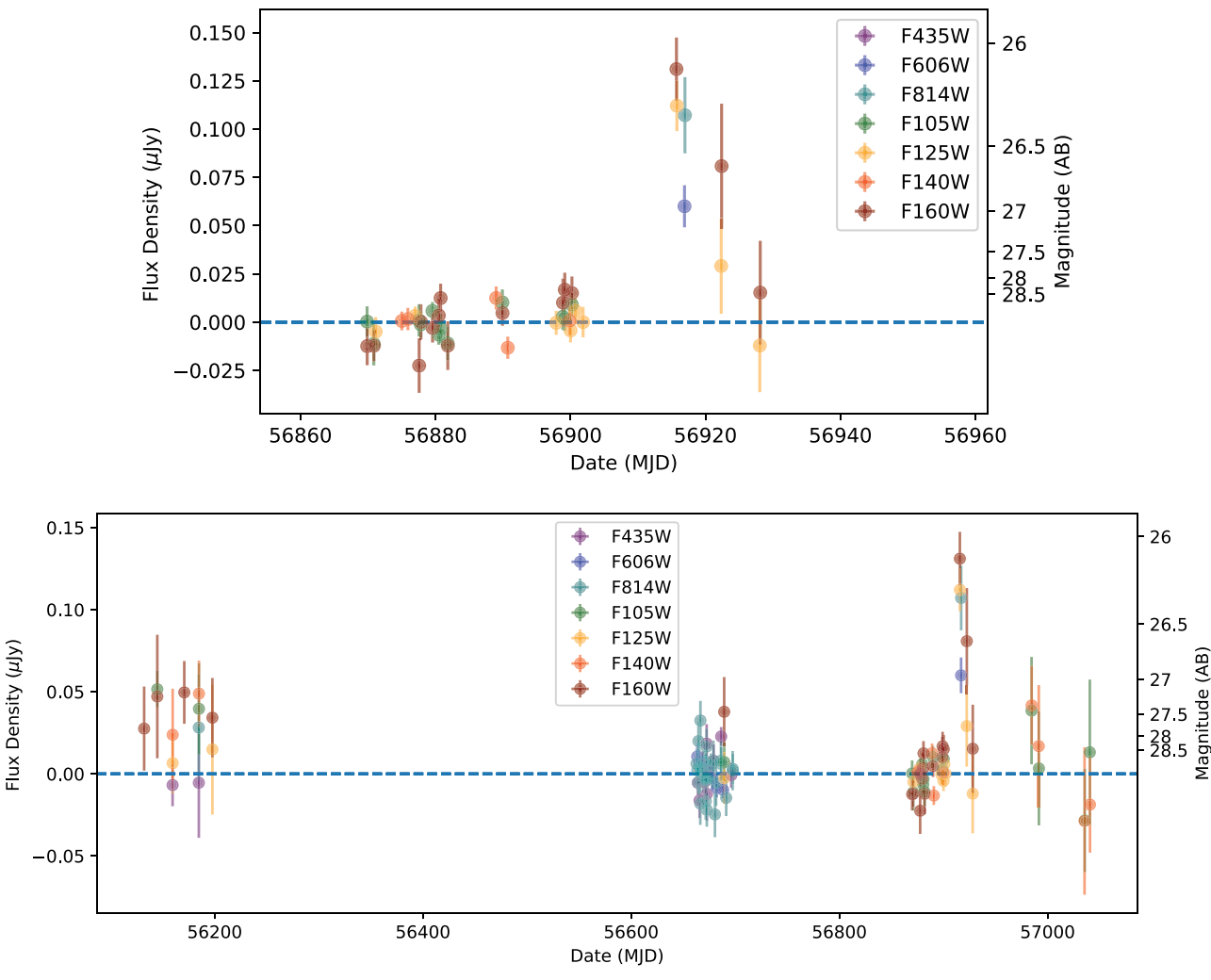


Figure 3. Photometry of the newly identified microlensing event identified in archival images of the MACS0416 HFF galaxy-cluster field. The upper panel shows the multiband optical and near-infrared light curve close to peak brightness in 2014 September, and shows that its timescale is on the order of several weeks, similar to those of the microlensing events reported by Kelly et al. (2018) in MACS1149 and Rodney et al. (2018) in MACS0416. A several-week duration is also consistent with the expected transverse velocities of galaxy clusters (Venumadhav et al. 2017; Diego et al. 2018; Kelly et al. 2018; Oguri et al. 2018). The lower panel plots all existing *HST* observations of the MACS0416 galaxy-cluster field.

archival *HST* imaging during the HFF project, as the true peak of this microlensing event may have occurred during gaps of *HST* visits, as shown in Figure 3. Photometry is measured using a 0."2 aperture (detailed values are listed in Table 1). The light curve may also exhibit slow changes over a period of years, as shown in the bottom panel of Figure 3, consistent with the level of microlensing expected from stars responsible for the intracluster light of the cluster.

A microlensing peak should have a duration roughly R/v, where R is the size of the lensed source and v is the transverse velocity of the lensing system. Given the $\sim 1000 \, \mathrm{km \ s^{-1}}$ expected relative transverse velocity between the galaxy cluster and background source (Watson et al. 2013), the several-week timescale of the microlensing peaks implies that the lensed sources can only extend for at most several tens of astronomical units. Consequently, the lensed systems must be stellar systems (e.g., single star or binary system) instead of a star cluster.

4.3. A Pair of Images

A magnified source close to a fold caustic of a foreground galaxy-cluster lens should appear as a pair of images on

opposite sides of the critical curve. In the absence of microlensing, which can alter the total magnification of each image, the counterimages should have equal brightness. Warhol's location, marked by the green circle labeled "A" in Figure 4, corresponds to a peak along the underlying arc in coadditions of HFF F606W and F814W imaging acquired before the microlensing event. To examine whether a counterimage of the underlying source may exist along the arc, we measured the flux inside of a 0."05 diameter aperture as we moved it along the arc. Figure 5 shows a second peak labeled "B" (much fainter than the peak A) along the underlying arc.

To assess the statistical significance of image B, we fit simultaneously the F606W and F814W coadded images of the arc in a 1.2×0.6 region using the GALFIT package (Peng et al. 2002). Although GALFIT was written for analysis of galaxy surface-brightness distributions, it has a flexible set of profiles that includes the King (1962), Sérsic (1963), and Moffat (1969) functions. We assume that the underlying arc consists of an unresolved stellar population and therefore can be modeled by a smoothly varying function. Furthermore, the arc's surface-brightness distribution should be symmetric on opposite sides of the critical curve. Consequently, the center of

 Table 1

 Photometry Measured from HST Imaging

Table 1 (Continued)

Photometry Measured from HST Imaging							
Date	Bandpass	Flux Density	σ				
(MJD)		(μ J y)	(μ J y)				
56159.53	ACS F435W	-0.0068	0.0129				
56184.75	ACS F435W	-0.0054	0.0336				
56663.91	ACS F435W	-0.0054	0.0080				
56665.62	ACS F435W	-0.0162	0.0109				
56668.55	ACS F435W	0.0055	0.0082				
56670.42	ACS F435W	-0.0049	0.0049				
56671.94	ACS F435W	0.0025	0.0083				
56672.47	ACS F435W	0.0184	0.0118				
56672.73	ACS F435W	-0.0123	0.0163				
56679.25	ACS F435W	0.0079	0.0099				
56686.41	ACS F435W	0.0227	0.0057				
56696.11	ACS F435W	-0.0008	0.0077				
56663.43	ACS F606W	0.0105	0.0083				
56665.36	ACS F606W	0.0073	0.0075				
56671.47	ACS F606W	0.0040	0.0074				
56678.25	ACS F606W	-0.0030	0.0071				
56682.10	ACS F606W	-0.0086	0.0059				
56688.21	ACS F606W	-0.0098	0.0052				
56916.89	ACS F606W	0.0600	0.0109				
56184.74	ACS F814W	0.0282	0.0326				
56662.65	ACS F814W	0.0062	0.0087				
56663.56	ACS F814W	0.0025	0.0122				
56664.43	ACS F814W	-0.0052	0.0118				
56664.56	ACS F814W	0.0199	0.0117				
56665.49	ACS F814W	0.0039	0.0152				
56666.35	ACS F814W	-0.0181	0.0130				
56666.49	ACS F814W	0.0325	0.0119				
56669.28	ACS F814W	0.0013	0.0128				
56670.61	ACS F814W	-0.0030	0.0122				
56671.16	ACS F814W	0.0078	0.0112				
56671.60	ACS F814W	-0.0167	0.0113				
56672.07	ACS F814W	-0.0040	0.0115				
56672.28	ACS F814W	0.0166	0.0110				
56672.60	ACS F814W	-0.0219	0.0103				
56672.87	ACS F814W	-0.0026	0.0117				
56676.58	ACS F814W	0.0050	0.0074				
56678.91	ACS F814W	0.0079	0.0124				
56680.44	ACS F814W	-0.0247	0.0139				
56681.50	ACS F814W	-0.0053	0.0143				
56686.15	ACS F814W	0.0080	0.0124				
56686.55	ACS F814W	0.0061	0.0102				
56691.20	ACS F814W	-0.0146	0.0111				
56697.44	ACS F814W	0.0020	0.0120				
56697.57	ACS F814W	0.0030	0.0094				
56916.96	ACS F814W	0.1072	0.0197				
56144.84	WFC3 F105W	0.0515	0.0111				
56184.88	WFC3 F105W	0.0396	0.0279				
56689.40	WFC3 F105W	0.0072	0.0117				
56869.77	WFC3 F105W	0.0003	0.0079				
56870.76	WFC3 F105W	-0.0113	0.0111				
56877.46	WFC3 F105W	0.0009	0.0084				
56877.73	WFC3 F105W	-0.0012	0.0068				
56879.46	WFC3 F105W	0.0058	0.0046				
56880.38	WFC3 F105W	-0.0065	0.0052				
56880.65	WFC3 F105W	-0.0033	0.0032				
56881.71	WFC3 F105W	-0.0033 -0.0110	0.0077				
56889.81	WFC3 F105W	0.0110	0.0067				
56898.77	WFC3 F105W	0.0102	0.0068				
56899.04	WFC3 F105W	0.0028	0.0061				
56900.10	WFC3 F105W	0.0010	0.0061				
56984.57	WFC3 F105W WFC3 F105W	0.0385	0.0001				
56991.60	WFC3 F105W WFC3 F105W	0.0333	0.0327				
50991.00	WECS FIRST	0.0055	0.0347				

WFC3 F105W

57035.58

-0.0284

Date (MID) Bandpass Flux Density (μJy) σ (μJy) 57040.55 WFC3 F105W 0.0131 0.0443 56159.60 WFC3 F125W 0.0065 0.0185 56197.79 WFC3 F125W 0.0149 0.0397 56889.34 WFC3 F125W -0.0026 0.0157 56871.04 WFC3 F125W -0.0049 0.0075 56876.93 WFC3 F125W -0.0003 0.0062 56899.97 WFC3 F125W -0.0003 0.0062 56899.97 WFC3 F125W -0.0043 0.0062 56901.83 WFC3 F125W 0.0059 0.0069 56915.76 WFC3 F125W 0.0000 0.0079 56915.76 WFC3 F125W 0.0291 0.0247 56922.33 WFC3 F125W 0.0291 0.0247 56928.05 WFC3 F125W -0.0121 0.0242 56159.62 WFC3 F140W 0.0489 0.0201 56874.94 WFC3 F140W 0.0489 0.0210 56875.87 WFC3 F140W 0.016				
57040.55 WFC3 F105W 0.0131 0.0443 56159.60 WFC3 F125W 0.0065 0.0185 56197.79 WFC3 F125W 0.0065 0.0185 56197.79 WFC3 F125W 0.0049 0.0397 56889.34 WFC3 F125W -0.0049 0.0075 56876.93 WFC3 F125W -0.0003 0.0062 56897.84 WFC3 F125W -0.0043 0.0062 56990.64 WFC3 F125W -0.0043 0.0062 56900.64 WFC3 F125W 0.0059 0.0069 56918.33 WFC3 F125W 0.0059 0.0062 56915.76 WFC3 F125W 0.00291 0.0247 56922.33 WFC3 F125W 0.0121 0.0247 56928.05 WFC3 F125W -0.0121 0.0242 56184.87 WFC3 F140W 0.0489 0.020 56874.94 WFC3 F140W 0.0489 0.020 56875.87 WFC3 F140W 0.0016 0.0058 56880.67 WFC3 F140W 0.0012 0.005	Date	Bandpass	Flux Density	σ
56159.60 WFC3 F125W 0.0065 0.0185 56197.79 WFC3 F125W 0.0149 0.0397 56689.34 WFC3 F125W -0.0026 0.0157 56871.04 WFC3 F125W -0.0049 0.0075 56876.93 WFC3 F125W 0.0003 0.0062 56899.84 WFC3 F125W -0.0003 0.0062 56990.64 WFC3 F125W -0.0009 0.0069 56901.83 WFC3 F125W 0.0000 0.0079 56915.76 WFC3 F125W 0.0000 0.0079 56922.33 WFC3 F125W 0.0291 0.0247 56184.87 WFC3 F140W 0.0238 0.0280 56184.87 WFC3 F140W 0.0489 0.0201 56874.94 WFC3 F140W 0.00489 0.0201 56888.95 WFC3 F140W 0.0016 0.0058 56890.67 WFC3 F140W 0.0016 0.0058 56899.84 WFC3 F140W 0.0049 0.0077 56899.84 WFC3 F140W 0.00496 0.0	(MJD)	•	(μJy)	(μJy)
56197.79 WFC3 F125W 0.0149 0.0397 56689.34 WFC3 F125W -0.0026 0.0157 56871.04 WFC3 F125W -0.0049 0.0075 56876.93 WFC3 F125W -0.0003 0.0062 56899.84 WFC3 F125W -0.0003 0.0062 56990.64 WFC3 F125W 0.00059 0.0069 56915.76 WFC3 F125W 0.0000 0.0079 56915.76 WFC3 F125W 0.0291 0.0247 56922.33 WFC3 F125W 0.0291 0.0242 56159.62 WFC3 F140W 0.0238 0.0280 56184.87 WFC3 F140W 0.0489 0.0201 56874.94 WFC3 F140W 0.0006 0.0048 56875.87 WFC3 F140W 0.0015 0.0055 56888.95 WFC3 F140W 0.0125 0.0060 56984.63 WFC3 F140W 0.0088 0.0077 56984.63 WFC3 F140W 0.0169 0.0372 57035.45 WFC3 F160W 0.0169 0.03	57040.55	WFC3 F105W	0.0131	0.0443
56689.34 WFC3 F125W -0.0026 0.0157 56871.04 WFC3 F125W -0.0049 0.0075 56876.93 WFC3 F125W 0.0033 0.0062 56899.84 WFC3 F125W -0.0003 0.0062 56990.64 WFC3 F125W -0.0059 0.0069 56901.83 WFC3 F125W 0.0000 0.0079 56915.76 WFC3 F125W 0.01121 0.0131 56922.33 WFC3 F125W 0.0291 0.0247 56928.05 WFC3 F125W -0.0121 0.0242 56159.62 WFC3 F140W 0.0489 0.0201 56874.94 WFC3 F140W 0.0048 0.0016 56875.87 WFC3 F140W 0.0016 0.0058 56889.95 WFC3 F140W 0.0016 0.0058 56889.84 WFC3 F140W 0.0016 0.0055 56899.84 WFC3 F140W 0.00125 0.0060 56984.63 WFC3 F140W 0.0169 0.0372 57035.45 WFC3 F160W 0.0169 0.	56159.60	WFC3 F125W	0.0065	0.0185
56871.04 WFC3 F125W -0.0049 0.0075 56876.93 WFC3 F125W 0.0033 0.0048 56899.84 WFC3 F125W -0.0003 0.0062 56899.97 WFC3 F125W -0.0059 0.0069 56900.64 WFC3 F125W 0.0000 0.0079 56901.83 WFC3 F125W 0.0000 0.0079 56915.76 WFC3 F125W 0.0291 0.0247 56922.33 WFC3 F125W -0.0121 0.0247 56928.05 WFC3 F125W -0.0121 0.0242 56184.87 WFC3 F140W 0.0489 0.0201 56874.94 WFC3 F140W 0.00489 0.0201 56875.87 WFC3 F140W 0.0016 0.0058 56888.95 WFC3 F140W 0.0016 0.0058 56884.63 WFC3 F140W 0.0008 0.0077 56994.63 WFC3 F140W 0.0169 0.0372 57035.45 WFC3 F140W 0.0169 0.0372 56132.22 WFC3 F160W 0.0441 0.0	56197.79	WFC3 F125W	0.0149	0.0397
56876.93 WFC3 F125W 0.0033 0.0048 56897.84 WFC3 F125W -0.0003 0.0062 56899.97 WFC3 F125W -0.0043 0.0062 56900.64 WFC3 F125W 0.0059 0.0069 56901.83 WFC3 F125W 0.0000 0.0079 56915.76 WFC3 F125W 0.1121 0.0131 56922.33 WFC3 F125W 0.0291 0.0247 56928.05 WFC3 F125W -0.0121 0.0242 56159.62 WFC3 F140W 0.0238 0.0280 56184.87 WFC3 F140W 0.00489 0.0201 56874.94 WFC3 F140W 0.0066 0.0048 56875.87 WFC3 F140W 0.0016 0.0058 56888.95 WFC3 F140W 0.0016 0.0058 56899.84 WFC3 F140W 0.008 0.0077 56991.47 WFC3 F140W 0.0169 0.0372 57035.45 WFC3 F140W 0.0169 0.0372 56132.22 WFC3 F160W 0.0471 0.0376	56689.34	WFC3 F125W	-0.0026	0.0157
56897.84 WFC3 F125W -0.0003 0.0062 56899.97 WFC3 F125W -0.0043 0.0062 56900.64 WFC3 F125W 0.0059 0.0069 56915.76 WFC3 F125W 0.0000 0.0079 56915.76 WFC3 F125W 0.0111 0.0241 56922.33 WFC3 F125W -0.0121 0.0242 56159.62 WFC3 F140W 0.0238 0.0280 56184.87 WFC3 F140W 0.00489 0.0201 56874.94 WFC3 F140W 0.0016 0.0058 56888.95 WFC3 F140W 0.0016 0.0058 56889.96 WFC3 F140W 0.00125 0.0060 56890.67 WFC3 F140W 0.0008 0.0077 56984.63 WFC3 F140W 0.00125 0.0060 56991.47 WFC3 F140W 0.0169 0.0372 56132.22 WFC3 F160W 0.0187 0.0249 56132.22 WFC3 F160W 0.0471 0.0376 5617.77 WFC3 F160W 0.0471 0.03	56871.04	WFC3 F125W	-0.0049	0.0075
56899.97 WFC3 F125W -0.0043 0.0062 56900.64 WFC3 F125W 0.0059 0.0069 56901.83 WFC3 F125W 0.0000 0.0079 56915.76 WFC3 F125W 0.1121 0.0131 56922.33 WFC3 F125W -0.0121 0.0247 56928.05 WFC3 F140W 0.0238 0.0280 56159.62 WFC3 F140W 0.0489 0.0201 56874.94 WFC3 F140W 0.0006 0.048 56875.87 WFC3 F140W 0.0016 0.0058 56888.95 WFC3 F140W 0.0125 0.0060 56890.67 WFC3 F140W -0.0133 0.0057 56899.84 WFC3 F140W 0.0008 0.0077 56984.63 WFC3 F140W 0.0169 0.0372 57035.45 WFC3 F140W -0.0187 0.0240 56132.22 WFC3 F160W -0.0187 0.0249 56144.86 WFC3 F160W 0.0471 0.0376 56197.77 WFC3 F160W 0.0496 0.019	56876.93	WFC3 F125W	0.0033	0.0048
56899.97 WFC3 F125W -0.0043 0.0062 56900.64 WFC3 F125W 0.0059 0.0069 56901.83 WFC3 F125W 0.0000 0.0079 56915.76 WFC3 F125W 0.1121 0.0131 56922.33 WFC3 F125W -0.0121 0.0247 56928.05 WFC3 F140W 0.0238 0.0280 56159.62 WFC3 F140W 0.0489 0.0201 56874.94 WFC3 F140W 0.0006 0.048 56875.87 WFC3 F140W 0.0016 0.0058 56888.95 WFC3 F140W 0.0125 0.0060 56890.67 WFC3 F140W -0.0133 0.0057 56899.84 WFC3 F140W 0.0008 0.0077 56984.63 WFC3 F140W 0.0169 0.0372 57035.45 WFC3 F140W -0.0187 0.0240 56132.22 WFC3 F160W -0.0187 0.0249 56144.86 WFC3 F160W 0.0471 0.0376 56197.77 WFC3 F160W 0.0496 0.019	56897.84	WFC3 F125W	-0.0003	0.0062
56901.83 WFC3 F125W 0.0000 0.0079 56915.76 WFC3 F125W 0.1121 0.0131 56922.33 WFC3 F125W 0.0291 0.0247 56928.05 WFC3 F125W -0.0121 0.0242 56159.62 WFC3 F140W 0.0288 0.0280 56184.87 WFC3 F140W 0.0489 0.0201 56874.94 WFC3 F140W 0.0006 0.0048 56875.87 WFC3 F140W 0.0016 0.0058 56888.95 WFC3 F140W 0.0125 0.0060 56890.67 WFC3 F140W -0.0133 0.0057 56898.4 WFC3 F140W 0.0008 0.0077 56984.63 WFC3 F140W 0.0169 0.0372 57035.45 WFC3 F140W -0.0187 0.0293 56132.22 WFC3 F160W -0.0187 0.0293 56144.86 WFC3 F160W 0.0471 0.0376 56197.77 WFC3 F160W 0.0378 0.0212 56880.78 WFC3 F160W -0.0124 0.009	56899.97		-0.0043	0.0062
56915.76 WFC3 F125W 0.1121 0.0131 56922.33 WFC3 F125W 0.0291 0.0247 56928.05 WFC3 F125W -0.0121 0.0242 56159.62 WFC3 F140W 0.0489 0.0201 56874.94 WFC3 F140W 0.0006 0.0048 56875.87 WFC3 F140W 0.0016 0.0058 56888.95 WFC3 F140W 0.0125 0.0060 56890.67 WFC3 F140W -0.0133 0.0057 56899.84 WFC3 F140W 0.0008 0.0077 56984.63 WFC3 F140W 0.00169 0.0372 57035.45 WFC3 F140W -0.0187 0.0240 56991.47 WFC3 F140W -0.0187 0.0293 56132.22 WFC3 F160W 0.0276 0.0256 56144.86 WFC3 F160W 0.0471 0.0372 56170.77 WFC3 F160W 0.0496 0.0191 56889.33 WFC3 F160W 0.0342 0.0241 56889.78 WFC3 F160W -0.0122 0.0	56900.64	WFC3 F125W	0.0059	0.0069
56922.33 WFC3 F125W 0.0291 0.0247 56928.05 WFC3 F125W -0.0121 0.0242 56159.62 WFC3 F140W 0.0238 0.0280 56184.87 WFC3 F140W 0.0489 0.0201 56874.94 WFC3 F140W 0.0006 0.0048 56875.87 WFC3 F140W 0.0016 0.0058 56888.95 WFC3 F140W 0.0125 0.0060 56890.67 WFC3 F140W 0.0008 0.0077 56898.43 WFC3 F140W 0.0008 0.0077 56991.47 WFC3 F140W 0.0169 0.0372 57035.45 WFC3 F140W -0.0287 0.0449 57040.62 WFC3 F140W -0.0187 0.0293 56132.22 WFC3 F160W 0.0471 0.0376 56170.77 WFC3 F160W 0.0471 0.0376 5689.33 WFC3 F160W 0.0342 0.0241 56869.78 WFC3 F160W -0.0124 0.0099 56877.48 WFC3 F160W -0.0030 0.007	56901.83	WFC3 F125W	0.0000	0.0079
56928.05 WFC3 F125W -0.0121 0.0242 56159.62 WFC3 F140W 0.0238 0.0280 56184.87 WFC3 F140W 0.0489 0.0201 56874.94 WFC3 F140W 0.0006 0.0048 56875.87 WFC3 F140W 0.0016 0.0058 56888.95 WFC3 F140W -0.0133 0.0057 56890.67 WFC3 F140W 0.0008 0.0077 56998.44 WFC3 F140W 0.0008 0.0077 56999.84 WFC3 F140W 0.0169 0.0372 56991.47 WFC3 F140W 0.0169 0.0372 57035.45 WFC3 F140W -0.0187 0.0249 57040.62 WFC3 F140W -0.0187 0.0293 56132.22 WFC3 F160W 0.0471 0.0376 56170.77 WFC3 F160W 0.0496 0.0191 56197.77 WFC3 F160W 0.0342 0.0241 5689.33 WFC3 F160W -0.0124 0.0099 56877.48 WFC3 F160W -0.0122 0.00	56915.76	WFC3 F125W	0.1121	0.0131
56159.62 WFC3 F140W 0.0238 0.0280 56184.87 WFC3 F140W 0.0489 0.0201 56874.94 WFC3 F140W 0.0006 0.0048 56875.87 WFC3 F140W 0.0016 0.0058 56888.95 WFC3 F140W 0.0125 0.0060 56890.67 WFC3 F140W -0.0133 0.0057 56899.84 WFC3 F140W 0.00417 0.0240 56991.47 WFC3 F140W 0.0169 0.0372 57035.45 WFC3 F140W -0.0187 0.0293 56132.22 WFC3 F160W -0.0187 0.0293 56144.86 WFC3 F160W 0.0471 0.0376 56197.77 WFC3 F160W 0.0496 0.0191 5689.33 WFC3 F160W 0.0378 0.0212 5687.8 WFC3 F160W -0.0124 0.0099 5687.48 WFC3 F160W -0.0122 0.0041 5687.7.48 WFC3 F160W -0.0030 0.0075 56880.40 WFC3 F160W 0.0034 0.009	56922.33	WFC3 F125W	0.0291	0.0247
56184.87 WFC3 F140W 0.0489 0.0201 56874.94 WFC3 F140W 0.0006 0.0048 56875.87 WFC3 F140W 0.0016 0.0058 56888.95 WFC3 F140W 0.0125 0.0060 56890.67 WFC3 F140W -0.0133 0.0057 56899.84 WFC3 F140W 0.0008 0.0077 56984.63 WFC3 F140W 0.0417 0.0240 56991.47 WFC3 F140W 0.0169 0.0372 57035.45 WFC3 F140W -0.0287 0.0449 57040.62 WFC3 F160W -0.0187 0.0293 56132.22 WFC3 F160W 0.0276 0.0256 56144.86 WFC3 F160W 0.0496 0.0191 56197.77 WFC3 F160W 0.0342 0.0241 5689.33 WFC3 F160W 0.0378 0.0212 5687.78 WFC3 F160W -0.0124 0.0099 5687.748 WFC3 F160W -0.0122 0.0081 56879.47 WFC3 F160W 0.0001 0.0075	56928.05	WFC3 F125W	-0.0121	0.0242
56874.94 WFC3 F140W 0.0006 0.0048 56875.87 WFC3 F140W 0.0016 0.0058 56888.95 WFC3 F140W 0.0125 0.0060 56890.67 WFC3 F140W -0.0133 0.0057 56899.84 WFC3 F140W 0.0008 0.0077 56984.63 WFC3 F140W 0.0417 0.0240 56991.47 WFC3 F140W 0.0169 0.0372 57035.45 WFC3 F140W -0.0287 0.0449 57040.62 WFC3 F160W -0.0187 0.0293 56132.22 WFC3 F160W 0.0276 0.0256 56144.86 WFC3 F160W 0.0496 0.0191 56197.77 WFC3 F160W 0.0342 0.0241 56689.33 WFC3 F160W 0.0378 0.0212 5687.78 WFC3 F160W -0.0124 0.0099 5687.78 WFC3 F160W -0.0122 0.0081 5687.47 WFC3 F160W -0.00225 0.0141 56879.47 WFC3 F160W -0.0030 0.00	56159.62	WFC3 F140W	0.0238	0.0280
56875.87 WFC3 F140W 0.0016 0.0058 56888.95 WFC3 F140W 0.0125 0.0060 56890.67 WFC3 F140W -0.0133 0.0057 56899.84 WFC3 F140W 0.0008 0.0077 56984.63 WFC3 F140W 0.0417 0.0240 56991.47 WFC3 F140W 0.0169 0.0372 57035.45 WFC3 F140W -0.0287 0.0449 57040.62 WFC3 F160W -0.0187 0.0293 56132.22 WFC3 F160W 0.0276 0.0256 56144.86 WFC3 F160W 0.0471 0.0376 56170.77 WFC3 F160W 0.0496 0.0191 5689.33 WFC3 F160W 0.0378 0.0212 5689.78 WFC3 F160W -0.0124 0.0099 5687.78 WFC3 F160W -0.0124 0.0099 5687.748 WFC3 F160W -0.0030 0.0075 56880.40 WFC3 F160W 0.0001 0.0091 56880.47 WFC3 F160W 0.0025 0.0075	56184.87	WFC3 F140W	0.0489	0.0201
56888.95 WFC3 F140W 0.0125 0.0060 56890.67 WFC3 F140W -0.0133 0.0057 56899.84 WFC3 F140W 0.0008 0.0077 56984.63 WFC3 F140W 0.0417 0.0240 56991.47 WFC3 F140W 0.0169 0.0372 57035.45 WFC3 F140W -0.0287 0.0449 57040.62 WFC3 F160W -0.0187 0.0293 56132.22 WFC3 F160W 0.0276 0.0256 56144.86 WFC3 F160W 0.0471 0.0376 56170.77 WFC3 F160W 0.0496 0.0191 56197.77 WFC3 F160W 0.0342 0.0241 56889.33 WFC3 F160W 0.0378 0.0212 56869.78 WFC3 F160W -0.0124 0.0099 56877.48 WFC3 F160W -0.0122 0.0081 56877.75 WFC3 F160W 0.0001 0.0091 56880.40 WFC3 F160W 0.0034 0.0095 56880.40 WFC3 F160W 0.0125 0.00	56874.94	WFC3 F140W		0.0048
56890.67 WFC3 F140W -0.0133 0.0057 56899.84 WFC3 F140W 0.0008 0.0077 56984.63 WFC3 F140W 0.0417 0.0240 56991.47 WFC3 F140W 0.0169 0.0372 57035.45 WFC3 F140W -0.0287 0.0449 57040.62 WFC3 F160W -0.0187 0.0293 56132.22 WFC3 F160W 0.0471 0.0376 56170.77 WFC3 F160W 0.0496 0.0191 56197.77 WFC3 F160W 0.0342 0.0241 56689.33 WFC3 F160W 0.0378 0.0212 56869.78 WFC3 F160W -0.0124 0.0099 56877.48 WFC3 F160W -0.0122 0.0081 56877.48 WFC3 F160W -0.0030 0.0075 56880.40 WFC3 F160W -0.0034 0.0091 56889.47 WFC3 F160W 0.0034 0.0090 56889.83 WFC3 F160W 0.0047 0.066 56889.83 WFC3 F160W 0.0047 0.0	56875.87	WFC3 F140W	0.0016	0.0058
56899.84 WFC3 F140W 0.0008 0.0077 56984.63 WFC3 F140W 0.0417 0.0240 56991.47 WFC3 F140W 0.0169 0.0372 57035.45 WFC3 F140W -0.0287 0.0449 57040.62 WFC3 F140W -0.0187 0.0293 56132.22 WFC3 F160W 0.0276 0.0256 56144.86 WFC3 F160W 0.0471 0.0376 56170.77 WFC3 F160W 0.0496 0.0191 56197.77 WFC3 F160W 0.0342 0.0241 56689.33 WFC3 F160W 0.0378 0.0212 56869.78 WFC3 F160W -0.0124 0.0099 56870.78 WFC3 F160W -0.0122 0.0081 56877.48 WFC3 F160W -0.00225 0.0141 56879.47 WFC3 F160W -0.0030 0.0075 56880.40 WFC3 F160W 0.0034 0.0090 56880.67 WFC3 F160W 0.0125 0.0126 56889.83 WFC3 F160W 0.0047 0.	56888.95	WFC3 F140W	0.0125	0.0060
56984.63 WFC3 F140W 0.0417 0.0240 56991.47 WFC3 F140W 0.0169 0.0372 57035.45 WFC3 F140W -0.0287 0.0449 57040.62 WFC3 F140W -0.0187 0.0293 56132.22 WFC3 F160W 0.0276 0.0256 56144.86 WFC3 F160W 0.0471 0.0376 56170.77 WFC3 F160W 0.0496 0.0191 56197.77 WFC3 F160W 0.0342 0.0241 56689.33 WFC3 F160W 0.0378 0.0212 56869.78 WFC3 F160W -0.0124 0.0099 56877.48 WFC3 F160W -0.0122 0.0081 56877.48 WFC3 F160W -0.0012 0.0014 56879.47 WFC3 F160W 0.0001 0.0091 56879.47 WFC3 F160W 0.0034 0.0090 56880.67 WFC3 F160W 0.0034 0.0090 56880.67 WFC3 F160W 0.0047 0.0066 56899.83 WFC3 F160W 0.0047 0.00	56890.67	WFC3 F140W	-0.0133	0.0057
56991.47 WFC3 F140W 0.0169 0.0372 57035.45 WFC3 F140W -0.0287 0.0449 57040.62 WFC3 F140W -0.0187 0.0293 56132.22 WFC3 F160W 0.0276 0.0256 56144.86 WFC3 F160W 0.0471 0.0376 56170.77 WFC3 F160W 0.0496 0.0191 56197.77 WFC3 F160W 0.0342 0.0241 56689.33 WFC3 F160W 0.0378 0.0212 56869.78 WFC3 F160W -0.0124 0.0099 56870.78 WFC3 F160W -0.0122 0.0081 56877.48 WFC3 F160W -0.00225 0.0141 56877.75 WFC3 F160W 0.0001 0.0091 56879.47 WFC3 F160W -0.0030 0.0075 56880.40 WFC3 F160W 0.0034 0.0090 56880.67 WFC3 F160W 0.0125 0.0075 56889.83 WFC3 F160W 0.0047 0.066 56899.06 WFC3 F160W 0.0168 0.0	56899.84	WFC3 F140W	0.0008	0.0077
57035.45 WFC3 F140W -0.0287 0.0449 57040.62 WFC3 F140W -0.0187 0.0293 56132.22 WFC3 F160W 0.0276 0.0256 56144.86 WFC3 F160W 0.0471 0.0376 56170.77 WFC3 F160W 0.0496 0.0191 56197.77 WFC3 F160W 0.0342 0.0241 56689.33 WFC3 F160W 0.0378 0.0212 56869.78 WFC3 F160W -0.0124 0.0099 56870.78 WFC3 F160W -0.0122 0.0081 56877.48 WFC3 F160W -0.00225 0.0141 56877.47 WFC3 F160W 0.0001 0.0091 56879.47 WFC3 F160W -0.0030 0.0075 56880.40 WFC3 F160W 0.0034 0.0090 56880.67 WFC3 F160W 0.0125 0.0075 56881.73 WFC3 F160W 0.0047 0.0066 56898.83 WFC3 F160W 0.0101 0.0125 56899.06 WFC3 F160W 0.0168 0.	56984.63	WFC3 F140W	0.0417	0.0240
57040.62 WFC3 F140W -0.0187 0.0293 56132.22 WFC3 F160W 0.0276 0.0256 56144.86 WFC3 F160W 0.0471 0.0376 56170.77 WFC3 F160W 0.0496 0.0191 56197.77 WFC3 F160W 0.0342 0.0241 56689.33 WFC3 F160W 0.0378 0.0212 56869.78 WFC3 F160W -0.0124 0.0099 56870.78 WFC3 F160W -0.0122 0.0081 56877.48 WFC3 F160W -0.00225 0.0141 56877.75 WFC3 F160W 0.0001 0.0091 56879.47 WFC3 F160W -0.0030 0.0075 56880.40 WFC3 F160W 0.0034 0.0090 56880.67 WFC3 F160W 0.0125 0.0075 56881.73 WFC3 F160W 0.0047 0.0066 56898.83 WFC3 F160W 0.0047 0.0066 56899.06 WFC3 F160W 0.0168 0.0088 56900.12 WFC3 F160W 0.0151 0.0	56991.47	WFC3 F140W	0.0169	0.0372
56132.22 WFC3 F160W 0.0276 0.0256 56144.86 WFC3 F160W 0.0471 0.0376 56170.77 WFC3 F160W 0.0496 0.0191 56197.77 WFC3 F160W 0.0342 0.0241 56689.33 WFC3 F160W 0.0378 0.0212 56869.78 WFC3 F160W -0.0124 0.0099 56870.78 WFC3 F160W -0.0122 0.0081 56877.48 WFC3 F160W -0.00225 0.0141 56877.75 WFC3 F160W 0.0001 0.0091 56879.47 WFC3 F160W -0.0030 0.0075 56880.40 WFC3 F160W 0.0034 0.0090 56880.67 WFC3 F160W 0.0125 0.0075 56881.73 WFC3 F160W 0.0047 0.0066 56898.83 WFC3 F160W 0.0047 0.0066 56898.79 WFC3 F160W 0.0168 0.0088 56900.12 WFC3 F160W 0.0151 0.0086 56915.70 WFC3 F160W 0.1311 0.01	57035.45	WFC3 F140W	-0.0287	0.0449
56144.86 WFC3 F160W 0.0471 0.0376 56170.77 WFC3 F160W 0.0496 0.0191 56197.77 WFC3 F160W 0.0342 0.0241 56689.33 WFC3 F160W 0.0378 0.0212 56869.78 WFC3 F160W -0.0124 0.0099 56870.78 WFC3 F160W -0.0122 0.0081 56877.48 WFC3 F160W -0.0225 0.0141 56877.75 WFC3 F160W 0.0001 0.0091 56879.47 WFC3 F160W -0.0030 0.0075 56880.40 WFC3 F160W 0.0034 0.0090 56880.67 WFC3 F160W 0.0125 0.0075 56881.73 WFC3 F160W -0.0122 0.0126 56898.83 WFC3 F160W 0.0047 0.0066 56899.06 WFC3 F160W 0.0101 0.0125 56899.06 WFC3 F160W 0.0168 0.0088 56915.70 WFC3 F160W 0.0151 0.0086 56922.39 WFC3 F160W 0.0808 0.03	57040.62	WFC3 F140W	-0.0187	0.0293
56170.77 WFC3 F160W 0.0496 0.0191 56197.77 WFC3 F160W 0.0342 0.0241 56689.33 WFC3 F160W 0.0378 0.0212 56869.78 WFC3 F160W -0.0124 0.0099 56870.78 WFC3 F160W -0.0122 0.0081 56877.48 WFC3 F160W -0.0225 0.0141 56877.75 WFC3 F160W 0.0001 0.0091 56879.47 WFC3 F160W -0.0030 0.0075 56880.40 WFC3 F160W 0.0034 0.0090 56880.67 WFC3 F160W 0.0125 0.0075 56881.73 WFC3 F160W -0.0122 0.0126 56898.83 WFC3 F160W 0.0047 0.0066 56898.79 WFC3 F160W 0.0101 0.0125 56899.06 WFC3 F160W 0.0168 0.0088 56900.12 WFC3 F160W 0.0151 0.0086 56915.70 WFC3 F160W 0.1311 0.0163 56922.39 WFC3 F160W 0.0808 0.03	56132.22	WFC3 F160W	0.0276	0.0256
56197.77 WFC3 F160W 0.0342 0.0241 56689.33 WFC3 F160W 0.0378 0.0212 56869.78 WFC3 F160W -0.0124 0.0099 56870.78 WFC3 F160W -0.0122 0.0081 56877.48 WFC3 F160W -0.0225 0.0141 56877.75 WFC3 F160W 0.0001 0.0091 56879.47 WFC3 F160W -0.0030 0.0075 56880.40 WFC3 F160W 0.0034 0.0090 56880.67 WFC3 F160W 0.0125 0.0075 56881.73 WFC3 F160W -0.0122 0.0126 56889.83 WFC3 F160W 0.0047 0.0066 56898.79 WFC3 F160W 0.0101 0.0125 56899.06 WFC3 F160W 0.0168 0.0088 56900.12 WFC3 F160W 0.0151 0.0086 56915.70 WFC3 F160W 0.1311 0.0163 56922.39 WFC3 F160W 0.0808 0.0323	56144.86	WFC3 F160W	0.0471	0.0376
56689.33 WFC3 F160W 0.0378 0.0212 56869.78 WFC3 F160W -0.0124 0.0099 56870.78 WFC3 F160W -0.0122 0.0081 56877.48 WFC3 F160W -0.0225 0.0141 56877.75 WFC3 F160W 0.0001 0.0091 56879.47 WFC3 F160W -0.0030 0.0075 56880.40 WFC3 F160W 0.0034 0.0090 56880.67 WFC3 F160W 0.0125 0.0075 56881.73 WFC3 F160W -0.0122 0.0126 56889.83 WFC3 F160W 0.0047 0.0066 56898.79 WFC3 F160W 0.0101 0.0125 56899.06 WFC3 F160W 0.0168 0.0088 56900.12 WFC3 F160W 0.0151 0.0086 56915.70 WFC3 F160W 0.1311 0.0163 56922.39 WFC3 F160W 0.0808 0.0323	56170.77	WFC3 F160W	0.0496	0.0191
56869.78 WFC3 F160W -0.0124 0.0099 56870.78 WFC3 F160W -0.0122 0.0081 56877.48 WFC3 F160W -0.0225 0.0141 56877.75 WFC3 F160W 0.0001 0.0091 56879.47 WFC3 F160W -0.0030 0.0075 56880.40 WFC3 F160W 0.0034 0.0090 56880.67 WFC3 F160W 0.0125 0.0075 56881.73 WFC3 F160W -0.0122 0.0126 56889.83 WFC3 F160W 0.0047 0.0066 56898.79 WFC3 F160W 0.0101 0.0125 56899.06 WFC3 F160W 0.0168 0.0088 56900.12 WFC3 F160W 0.0151 0.0086 56915.70 WFC3 F160W 0.1311 0.0163 56922.39 WFC3 F160W 0.0808 0.0323	56197.77	WFC3 F160W	0.0342	0.0241
56870.78 WFC3 F160W -0.0122 0.0081 56877.48 WFC3 F160W -0.0225 0.0141 56877.75 WFC3 F160W 0.0001 0.0091 56879.47 WFC3 F160W -0.0030 0.0075 56880.40 WFC3 F160W 0.0034 0.0090 56880.67 WFC3 F160W 0.0125 0.0075 56881.73 WFC3 F160W -0.0122 0.0126 56889.83 WFC3 F160W 0.0047 0.0066 56898.79 WFC3 F160W 0.0101 0.0125 56899.06 WFC3 F160W 0.0168 0.0088 56900.12 WFC3 F160W 0.0151 0.0086 56915.70 WFC3 F160W 0.1311 0.0163 56922.39 WFC3 F160W 0.0808 0.0323	56689.33	WFC3 F160W	0.0378	0.0212
56877.48 WFC3 F160W -0.0225 0.0141 56877.75 WFC3 F160W 0.0001 0.0091 56879.47 WFC3 F160W -0.0030 0.0075 56880.40 WFC3 F160W 0.0034 0.0090 56880.67 WFC3 F160W 0.0125 0.0075 56881.73 WFC3 F160W -0.0122 0.0126 56889.83 WFC3 F160W 0.0047 0.0066 56898.79 WFC3 F160W 0.0101 0.0125 56899.06 WFC3 F160W 0.0168 0.0088 56900.12 WFC3 F160W 0.0151 0.0086 56915.70 WFC3 F160W 0.1311 0.0163 56922.39 WFC3 F160W 0.0808 0.0323	56869.78	WFC3 F160W	-0.0124	0.0099
56877.75 WFC3 F160W 0.0001 0.0091 56879.47 WFC3 F160W -0.0030 0.0075 56880.40 WFC3 F160W 0.0034 0.0090 56880.67 WFC3 F160W 0.0125 0.0075 56881.73 WFC3 F160W -0.0122 0.0126 56889.83 WFC3 F160W 0.0047 0.0066 56898.79 WFC3 F160W 0.0101 0.0125 56899.06 WFC3 F160W 0.0168 0.0088 56900.12 WFC3 F160W 0.0151 0.0086 56915.70 WFC3 F160W 0.1311 0.0163 56922.39 WFC3 F160W 0.0808 0.0323	56870.78	WFC3 F160W	-0.0122	0.0081
56879.47 WFC3 F160W -0.0030 0.0075 56880.40 WFC3 F160W 0.0034 0.0090 56880.67 WFC3 F160W 0.0125 0.0075 56881.73 WFC3 F160W -0.0122 0.0126 56889.83 WFC3 F160W 0.0047 0.0066 56898.79 WFC3 F160W 0.0101 0.0125 56899.06 WFC3 F160W 0.0168 0.0088 56900.12 WFC3 F160W 0.0151 0.0086 56915.70 WFC3 F160W 0.1311 0.0163 56922.39 WFC3 F160W 0.0808 0.0323	56877.48	WFC3 F160W	-0.0225	0.0141
56880.40 WFC3 F160W 0.0034 0.0090 56880.67 WFC3 F160W 0.0125 0.0075 56881.73 WFC3 F160W -0.0122 0.0126 56889.83 WFC3 F160W 0.0047 0.0066 56898.79 WFC3 F160W 0.0101 0.0125 56899.06 WFC3 F160W 0.0168 0.0088 56900.12 WFC3 F160W 0.0151 0.0086 56915.70 WFC3 F160W 0.1311 0.0163 56922.39 WFC3 F160W 0.0808 0.0323	56877.75	WFC3 F160W	0.0001	0.0091
56880.67 WFC3 F160W 0.0125 0.0075 56881.73 WFC3 F160W -0.0122 0.0126 56889.83 WFC3 F160W 0.0047 0.0066 56898.79 WFC3 F160W 0.0101 0.0125 56899.06 WFC3 F160W 0.0168 0.0088 56900.12 WFC3 F160W 0.0151 0.0086 56915.70 WFC3 F160W 0.1311 0.0163 56922.39 WFC3 F160W 0.0808 0.0323	56879.47	WFC3 F160W	-0.0030	0.0075
56881.73 WFC3 F160W -0.0122 0.0126 56889.83 WFC3 F160W 0.0047 0.0066 56898.79 WFC3 F160W 0.0101 0.0125 56899.06 WFC3 F160W 0.0168 0.0088 56900.12 WFC3 F160W 0.0151 0.0086 56915.70 WFC3 F160W 0.1311 0.0163 56922.39 WFC3 F160W 0.0808 0.0323	56880.40	WFC3 F160W	0.0034	0.0090
56889.83 WFC3 F160W 0.0047 0.0066 56898.79 WFC3 F160W 0.0101 0.0125 56899.06 WFC3 F160W 0.0168 0.0088 56900.12 WFC3 F160W 0.0151 0.0086 56915.70 WFC3 F160W 0.1311 0.0163 56922.39 WFC3 F160W 0.0808 0.0323	56880.67	WFC3 F160W	0.0125	0.0075
56898.79 WFC3 F160W 0.0101 0.0125 56899.06 WFC3 F160W 0.0168 0.0088 56900.12 WFC3 F160W 0.0151 0.0086 56915.70 WFC3 F160W 0.1311 0.0163 56922.39 WFC3 F160W 0.0808 0.0323	56881.73	WFC3 F160W	-0.0122	0.0126
56899.06 WFC3 F160W 0.0168 0.0088 56900.12 WFC3 F160W 0.0151 0.0086 56915.70 WFC3 F160W 0.1311 0.0163 56922.39 WFC3 F160W 0.0808 0.0323	56889.83	WFC3 F160W	0.0047	0.0066
56900.12 WFC3 F160W 0.0151 0.0086 56915.70 WFC3 F160W 0.1311 0.0163 56922.39 WFC3 F160W 0.0808 0.0323	56898.79	WFC3 F160W	0.0101	0.0125
56915.70 WFC3 F160W 0.1311 0.0163 56922.39 WFC3 F160W 0.0808 0.0323	56899.06	WFC3 F160W	0.0168	0.0088
56922.39 WFC3 F160W 0.0808 0.0323	56900.12	WFC3 F160W	0.0151	0.0086
	56915.70	WFC3 F160W	0.1311	0.0163
56928.12 WFC3 F160W 0.0153 0.0268	56922.39	WFC3 F160W	0.0808	0.0323
	56928.12	WFC3 F160W	0.0153	0.0268

the component corresponding to the unresolved arc is set fixed to the location between images A and B.

We next fit a series of models to the arc. The first set of models consists of a component corresponding to the smoothly varying arc and a point source at the position of image A. Functions used for the smoothly varying arc include King, Sérsic, and Moffat profiles. In the next step, we modify these models by adding a second point source, at the location of the putative image B, and fit this model that includes image B to the same data.

For each model, we fit jointly the F606W and F814W imaging acquired before 2014 September, using all possible profile functions provided by GALFIT. Figure 6 shows Warhol's F606W and F814W deep HFF images, models, and residuals from the best-fitting model. To be able to perform

0.0316

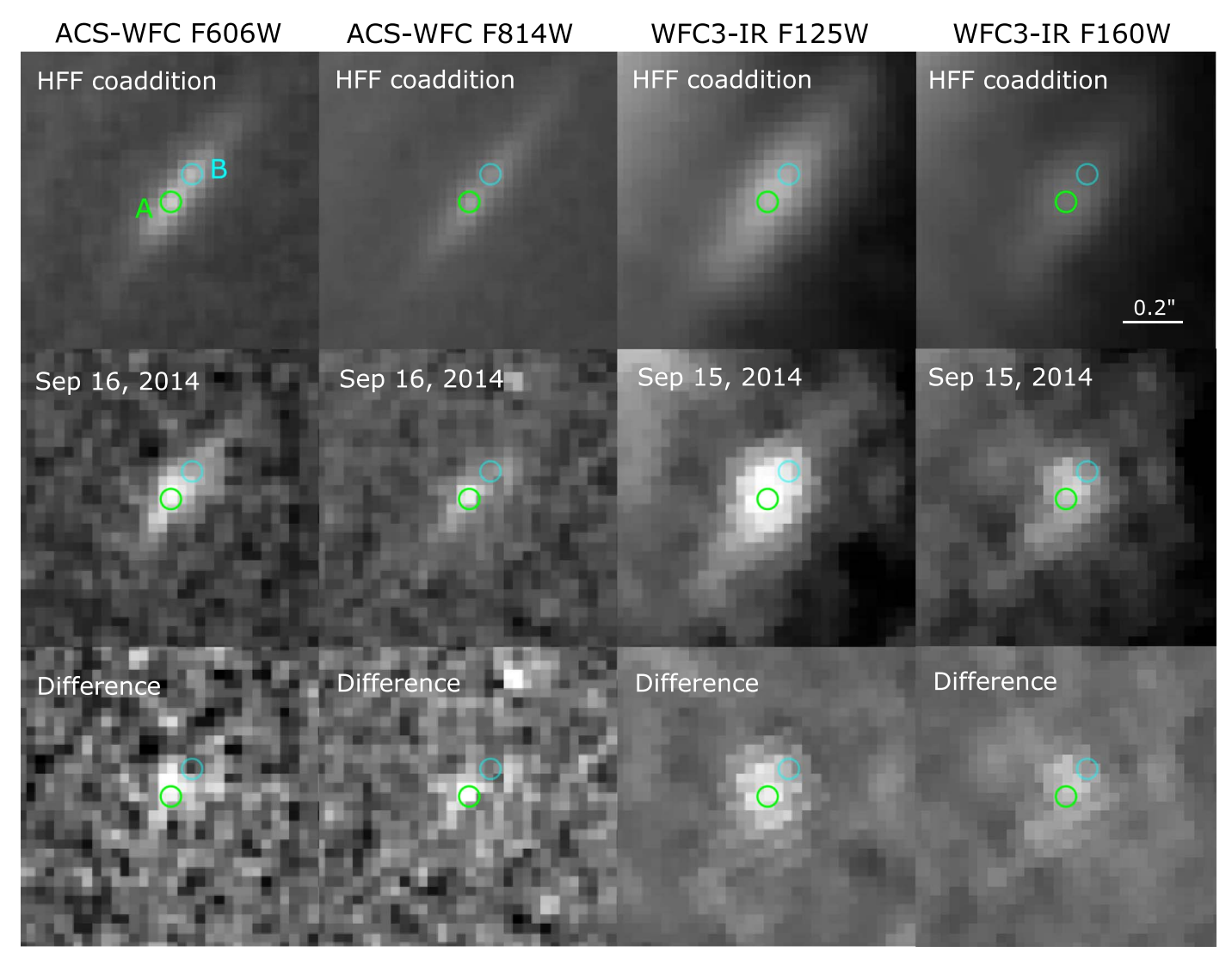


Figure 4. *HST* imaging around Warhol's position. Upper four panels show coadditions of *HST* images obtained from the HFF project using ACS-WFC F606W, ACS-WFC F814W, WFC3-IR F125W, and WFC3-IR F160W (templates). Middle four panels are the *HST* images during the microlensing event detected around 2014 September 15. Lower four panels are the difference images. A peak (marked by the circle "A" in the top left panel) can be identified from the optical *HST* imaging in the arc. There may be another peak along the arc shown in the F606W band (as marked by the circle "B"). The same positions of A and B are marked by green and cyan circles (respectively) in all images. Each pair of transient and template images is displayed using the same color scale.

model comparison, we evaluate the Akaike information criterion (AIC; Akaike 1974) from the best-fit results provided by the two models, as listed in Table 2. The result gives $\rm AIC_{single-peak} - \rm AIC_{two-peak} > 20$, indicating that the single-peak model has relatively "no empirical support" (Burnham et al. 2011) compared to the two-peak model. The best-fit result given by the two-peak model indicates that the AB magnitudes of source A and source B are 28.7 ± 0.1 and 29.4 ± 0.2 (respectively) in the ACS-WFC F606W band, and 28.53 ± 0.06 and 29.9 ± 0.3 in the ACS-WFC F814W band.

4.4. A Single Transient

Sources near a cluster fold caustic (with no microlenses) should appear as a pair of images with equal magnification. Therefore, if the new transient were a stellar outburst, we would expect to see a pair of transients with a relative time delay of less than a day. The outbursts of luminous stars persist for longer than a single day, and, as shown in Figure 3, Warhol had a duration of least two weeks. By contrast, a microlensing

event should only appear as a single transient, as a star or remnant in the cluster becomes temporarily aligned with one of the magnified images of the background star. Our GALFIT analysis finds that image B is, on average, ~ 1 mag fainter than image A, a difference that can be attributed to microlensing. Consequently, if the peak observed at image A's location were a stellar outburst, it would have also appeared at image B's position with a flux that was ~ 1 mag fainter. Given the peak fluxes of image A, the peak at image B's position would have had F814W ≈ 27.3 mag, F125W ≈ 27.3 mag, and F160W ≈ 27.1 mag, and these would have been detected with $\sim 2.1\sigma$, $\sim 3.4\sigma$, and $\sim 3.2\sigma$ significance. However, no evidence for a peak at image B's position is apparent in difference images, as shown in Figure 4.

4.5. Galaxy-cluster Models

We calculate magnification maps at z=0.94 using 10 independent Frontier Fields Lens Models (Lotz et al. 2017) for the MACS0416 galaxy cluster, as shown in Figure 2. The

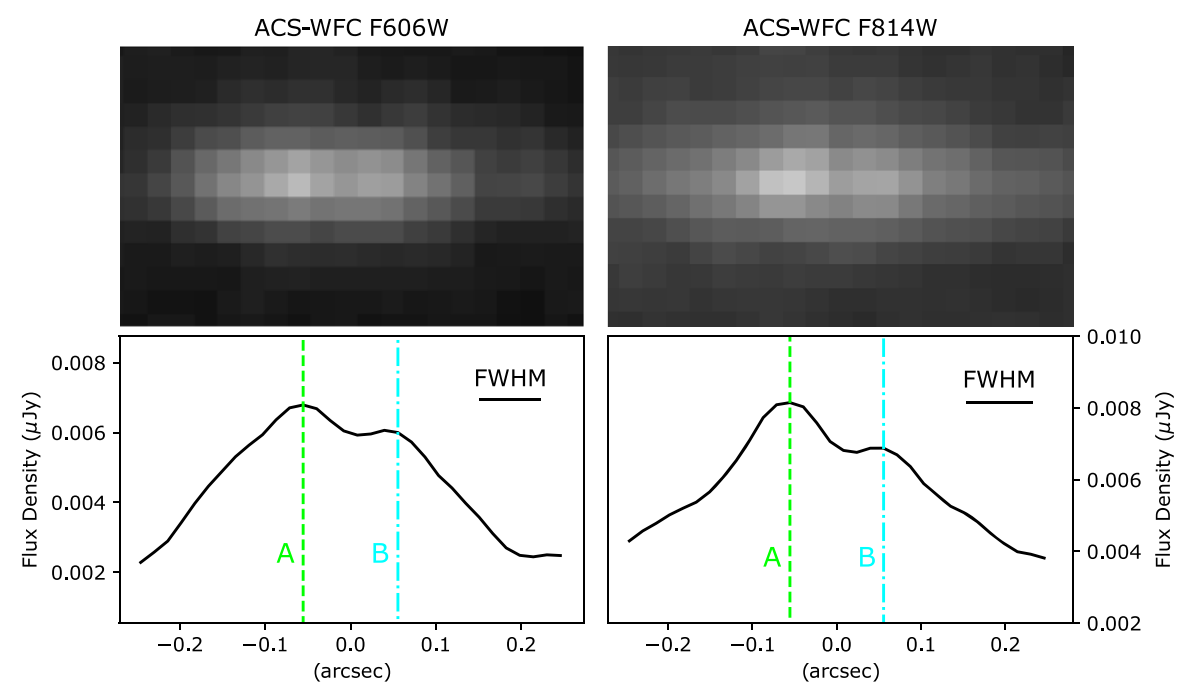


Figure 5. ACS-WFC F606W and ACS-WFC F814W imaging of the underlying arc detected by the HFF project before 2014 September 15–16. Bottom two panels show flux densities along the arc with a 0.005 diameter aperture. Vertical green and cyan lines show the positions A and B (respectively) in Figure 4. The horizontal bars show the FWHM of averaged PSFs in the ACS-WFC F606W and ACS-WFC F814W bands.

Table 2
Comparison between GALFIT Models Including Underlying Arc and One or Two Stellar Images Fit Simultaneously to F606W and F814W Coadded Images

Two-peak Model			Single-peak Model			
Profile	ΔAIC^a	χ^2_{ν}	Profile	ΔAIC	χ^2_{ν}	
Moffat	0	1.073	King	20.78	1.087	
King	2.77	1.075	Moffat	23.91	1.089	
Sérsic	4.82	1.076	Sérsic	28.48	1.092	

Note. Models in the left column include point source at positions A and B, and those in the right column include only a source at position A. The differences between the Akaike information criterion (AIC) imply that the single-image models have "no empirical support" (Burnham et al. 2011) compared to those that include a pair of images.

predicted magnification μ due to the galaxy-cluster lens at Warhol's position is listed in Table 3. In general, the locations of galaxy-cluster critical curves are constrained by current models to within a tenth of an arcsecond in the best cases. Given Warhol's proximity to the critical curve, the uncertainty in the critical curve's location results in a large magnification uncertainty at its position.

We compute the offsets between models' predictions for the location of the critical curve and the midpoint of the line between counterimages A and B (θ_c), as listed in Table 3. The offsets show that a majority of published lensing models place the critical curve within 0."3 of the midpoint. The Bradač (v3) and CATS (v4) models locate the critical curve at the greatest offset (>0."5) from the midpoint. The Zitrin-nfw (v3) model's predicted critical curve yields the smallest offset (0."02).

4.6. Fitting the Star's SED

After correcting for extinction expected for the Galactic foreground ($A_V = 0.112$ mag; Schlafly & Finkbeiner 2011), we

fit the SED of the microlensing peak. ACS-WFC F606W and F814W, as well as WFC-IR F125W and F160W, imaging was acquired during a first epoch on 2014 September 15–16; the optical and IR integrations were interspersed with each other in time. As shown in Figure 3, the transient was still detected during a second imaging epoch on 2014 September 22.

We simultaneously fit a Castelli & Kurucz (2004) stellar atmosphere model and a host-galaxy extinction curve to the measured SED of the Warhol microlensing event. We assume that the source did not vary significantly while the optical and IR images were acquired during the first epoch. We include as a fit parameter the change in the magnification (relative normalization of the SED) between the first and second epochs. Given the Patrício et al. (2018) measured abundance of $12 + \log(O/H) = 8.72 \pm 0.6$ dex, we use stellar models that have a solar abundance.

Figure 7 shows the best fits to the measured photometry when we allow the temperature of the stellar photosphere to vary as a free parameter. For a Milky Way (R(V) = 3.1;Cardelli et al. 1989) extinction law, we find a best-fitting temperature of 22,500 K, consistent with an early B-type star. Instead, adopting the extinction law for the Small Magellanic Cloud (SMC; R(V) = 2.73; Gordon et al. 2003) yields 23,700 K. We expect that microlensing may only potentially be chromatic when a microcaustic is close to the limb of the star, but this should occur over a very short timescale, smaller than the \sim 2 days during which observations near peak were acquired. While the surface gravity of early-type blue supergiants has values of $\log g \approx 2-2.8$ (e.g., Urbaneja et al. 2005; Przybilla et al. 2010), the Castelli & Kurucz (2004) models have $\log g \geqslant 3$ for photospheric temperatures exceeding 20,000 K, and this limitation may have some effect on the value of the inferred photospheric temperature.

The low to moderate best-fitting host-galaxy dust extinction is consistent with the $A_V=0.15\pm0.20\,\mathrm{mag}$ extinction inferred by Patrício et al. (2018) from an analysis of nebular emission lines from the lensed galaxy.

^a $\Delta AIC = AIC - AIC_{min}$.

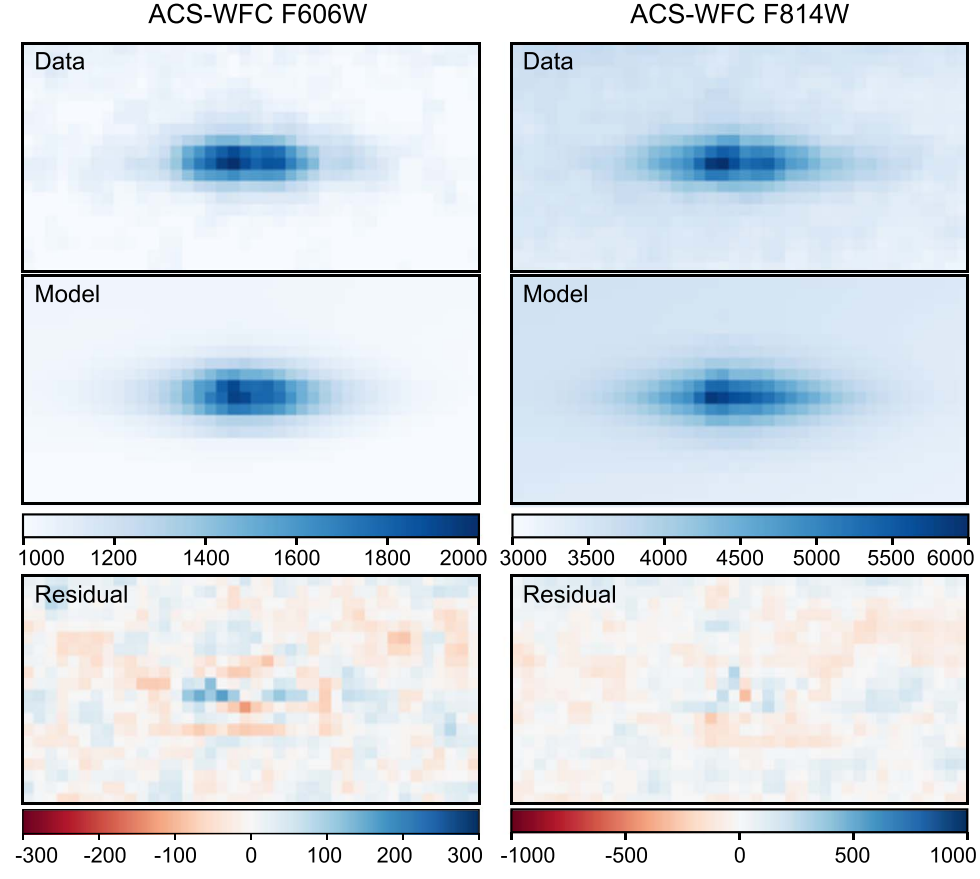


Figure 6. ACS-WFC F606W and ACS-WFC F814W imaging of the underlying arc detected by the HFF project before 2014 September. Top: original data (in units of photon counts). Middle: best-fit results using the GALFIT model with two point sources at positions A and B as shown in Figure 5. Bottom: residual.

Model	θ_c (")	μ	μ'	dθ (")	References
Bradač (v3)	-1.4	11	197	0.18	Bradač et al. (2005, 2009), Hoag et al. (2016)
Caminha (v4)	0.23	56	205	0.06	Caminha et al. (2017)
CATS (v4.1)	0.64	15	201	0.3	Jauzac et al. (2012, 2014), Richard et al. (2014)
Diego (v4.1)	0.34	25	250	0.42	Diego et al. (2005a, 2005b, 2007, 2015)
GLAFIC (v4)	-0.24	45	180 ^b	0.03	Oguri (2010), Kawamata et al. (2016, 2018)
Keeton (v4)	-0.05	369	304	0.06	Keeton (2010), Ammons et al. (2014), McCully et al. (2014)
Sharon (v4 Cor.)	0.35	40	228	0.05	Jullo et al. (2007), Johnson et al. (2014)
Williams/GRALE (v4)	0.43 ^b	40 ^b	250 ^b	N/A^b	Liesenborgs et al. (2006), Sebesta et al. (2016)
Zitrin-ltm-Gauss (v3)	0.21	100	331	0.06	Zitrin et al. (2009, 2013) (see also Merten et al. 2009, 2011)
Zitrin-nfw (v3)	-0.02	348	208	0.06	Zitrin et al. (2009, 2013) (see also Merten et al. 2009, 2011)

Notes. A positive offset (i.e., $\theta_c > 0$) indicates the transient locates on the northwest side of the critical curve.

4.7. Luminosity and Magnification of Lensed Star

We next estimate approximately the star's luminosity from the apparent magnitude of image A during HFF observations prior to the 2014 September microlensing event. To determine the star's magnification, we first compute a K-correction K_{xy} as

$$m_{y} = M_{x} + dm + K_{xy}, \tag{1}$$

where m_y is the observer-frame apparent magnitude in the y band, M_x is the rest-frame absolute magnitude in the x band,

and dm is the distance modulus. To calculate a K-correction, we use Equation (2) of Kim et al. (1996),

$$K = 2.5 \log_{10}(1+z) + m_{y,\text{syn}}^{\text{AB}} - m_{V,\text{syn}}^{\text{Vega}},$$
 (2)

where z=0.94, $m_{y,\rm syn}^{\rm AB}$ is the synthetic magnitude of a redshifted model spectrum in an observer-frame y band (e.g., ACS-WFC F814W), and $m_{V,\rm syn}^{\rm Vega}$ is the synthetic Johnson V-band magnitude of the rest-frame model spectrum. Using the best-fitting spectral models, we calculate $K_{V,F814W}\approx -1.2$ and

^a Magnifications predicted by MACS J0416.1-2403 lensing models. Those at the transient's coordinates show high dispersion given the uncertainty in the location of the galaxy cluster's critical curve.

^b Obtained from a map constructed from analytic basis functions instead of the published HFF models.

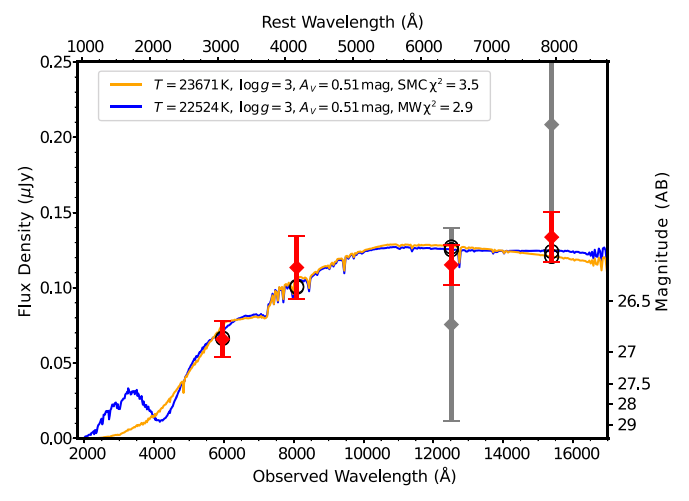


Figure 7. Stellar atmosphere model fits to the measured SED during the 2014 September microlensing event. For solar metallicity models and an MW (R(V) = 3.1; Cardelli et al. 1989) extinction law, the best-fitting temperature is 22,500 K, consistent with an early B-type star. Assuming instead an extinction law for the SMC (R(V) = 2.73; Gordon et al. 2003) yields a hotter best-fitting photospheric temperature of 23,700 K. Early-type blue supergiants have a surface gravity of $\log g \approx 2-2.8$ (e.g., Urbaneja et al. 2005; Przybilla et al. 2010), but the Castelli & Kurucz (2004) models we use are limited to $\log g \geqslant 3$ for photospheric temperatures exceeding 20,000 K, which may affect the precise value of the inferred photospheric temperature. The red points mark photometry measured from images taken on 2014 September 15 and 16. The gray points mark flux densities measured from imaging acquired on 2014 September 22; given the light curve's evolution we include an additional parameter in the fit: the relative flux normalization of the event between September 15–16 and September 22.

 $K_{V,F125W} \approx -0.4$, and adopt $dm = 43.96 \,\text{mag}$ at z = 0.94 (with no correction for magnification).

We have found that, during HFF observations before the microlensing peak, image A had an average ACS-WFC F814W magnitude of \sim 28.5. For an early B-type supergiant star with photospheric temperature of 22,400 K (B1V) from the Pickles (1998) library and $M_V = -8.3$ mag and without dust extinction, a magnification of \sim 266 would be implied. Such a magnification at images A's and B's separation from the critical curve is consistent with those expected from the existing lens models of the cluster listed in Table 3. The luminosities of blue supergiant stars in the SMC reach $M_V \gtrsim -8.8$ mag (Dachs 1970).

There are examples of extremely luminous, main-sequence O-type stars such as Melnick 34 in the 30 Doradus complex in the Large Magellanic Cloud (LMC) with an absolute magnitude of $M_V = -7.9$ mag (Doran et al. 2013). However, such very luminous O-type stars or Wolf–Rayet stars showing H in their spectra (WNH; Smith & Conti 2008) are extremely rare in comparison to cooler B-type supergiants at lower bolometric luminosity but similar M_V .

For example, Figure 3 of Fitzpatrick & Garmany (1990) presents a Hertzsprung–Russell diagram of the luminous stellar population of the LMC. After removing the bolometric corrections listed in Tables 1 and 2 of Fitzpatrick & Garmany (1990; see also Figure 6 of Flower 1996), we find that there are \sim 25 B-type supergiants (10,000 $\lesssim T \lesssim$ 30,000 K) but no O-type stars (\gtrsim 30,000 K) having $M_V \lesssim -8$ mag in the LMC. The comparatively small abundance of WNH stars arises from their initial masses (very approximately $100~M_{\odot}$ versus 10– $20~M_{\odot}$), but also the significantly longer lifetimes at the lower masses. Among

Table 4 Magnification (μ) Required for Different Types of Stars^a

	Spec. Model	Temp	M_V	F125W	K	μ
BSG	B8V	11749K	-8.5	34.94	-0.52	3003
Extreme MS	O5V	39810K	-8	35.58	-0.39	5381
MS	O5V	39810K	-5.40	38.18	-0.39	59002
MS	O9V	35481K	-4.00	39.60	-0.37	218257
MS	B0V	28183K	-3.70	39.87	-0.39	280249
MS	B1V	22387K	-3.20	40.33	-0.43	429719
MS	B3V	19054K	-2.10	41.41	-0.45	1163781
MS	B5-	14125K	-2.10	41.38	-0.48	1126591
	7V					
MS	B8V	11749K	-1.08	42.36	-0.52	2789947

Note

binary stars, blue supergiants can also be blue stragglers from mass gainers and mergers.

We have found that a B-type star with $A_V \approx 0.5$ mag provides the best fit to the SED of the microlensing event with the Castelli & Kurucz (2004) library. Our estimate of the star's absolute magnitude from the HFF imaging implies that it is highly luminous at rest-frame optical wavelengths, and indicates that it is a blue supergiant, given the comparatively small numbers of O-type stars with $M_V \lesssim -8$ mag. For reference, we list in Table 4 the magnifications that would be required for both main-sequence and post-main-sequence stars of different spectroscopic types to yield the *peak* observed magnitude of F125W ≈ 26.25 during the 2014 September microlensing event.

Blue supergiant stars would require magnifications that are factors of ten to hundreds smaller than typical main-sequence stars. For fold caustics, assuming the lens has a smooth mass distribution, the magnification μ decreases with the distance d in the source plane from the caustic as $\mu \propto d^{-1/2}$. Hence, the source-plane area A within which the magnification exceeds μ scales as $A(>\mu) \propto \mu^{-2}$, which implies that the magnifications needed for typical main-sequence will be much less common. Indeed, the presence of stars responsible for the intracluster light along the line of sight precludes almost all main-sequence stars, because stellar microlenses cause magnification exceeding 20,000 to become extremely unlikely (Diego 2019).

4.8. Constraints on Source Size

We next show that stellar microlensing can be expected at Warhol's offset from the critical curve, and that the timescale of the 2014 September microlensing event indicates that the lensed source corresponds to an individual star or stellar system. The separation between A and its possible counterimage B is \sim 0." 12. Near the critical curve, the GLAFIC galaxy-cluster mass model yields the following magnification for each

^a Approximate peak magnifications are for no host-galaxy extinction and for the peak observed F125W magnitude of ~26.25. "MS" is an abbreviation for main sequence, and "BSG" is an abbreviation for blue supergiant. Note that high magnifications are required for typical main-sequence stars using Pickles (1998) templates. Consequently, we favor a post-main-sequence blue supergiant having $-9 \lesssim M_V \lesssim -7$, although an extreme and even less common O-type main-sequence star also provides a satisfactory fit to the SED (see Figure 7).

of the images, in the case of a smooth model (i.e., with no microlensing):

$$\mu_{\text{each}} \approx (11'')/\theta_h,$$
 (3)

where θ_h is the angular distance from the critical curve. At an offset of $\theta_h \approx 0.006$ from the galaxy-cluster critical curve, $\mu_{\rm each} \approx 180$ ($\mu_t \approx 120$, $\mu_r \approx 1.5$), which may be a plausible location for caustic crossing given the saturation argument presented by Diego et al. (2018).

We also compute the source crossing time as

$$t_{\rm src} \approx 0.031 \frac{R_{\rm source}/R_{\odot}}{\nu/(500 \,{\rm km \, s^{-1}})} \,{\rm days},$$
 (4)

where v is a transverse velocity of the cluster and $R_{\rm source}$ is a radius of a background star that is magnified. From the light curve, we have $t_{\rm src} < 10$ days (see Figure 2 of Miralda-Escude 1991 to see how $t_{\rm src}$ relates to the expected timescale of the light curve's evolution), which yields a limit of $R_{\rm source} < 320\,R_{\odot}$. Assuming $\mu_t = 120$ and $\mu_r = 1.5$, the maximum magnification estimated using Equation (48) of Oguri et al. (2018) is

$$\mu_{\text{max}} \approx (4.5 \times 10^4) (M_{\text{lens}}/M_{\odot})^{1/4} (R_{\text{source}}/R_{\odot})^{-1/2}.$$
 (5)

For $M_{\rm lens}=0.3M_{\odot}$ (typical mass of a star responsible for the intracluster light of the cluster), we have $\mu_{\rm max}\approx 33{,}000$ for $R_{\rm source}=1\,R_{\odot},~\mu_{\rm max}\approx 10{,}000$ for $R_{\rm source}=10\,R_{\odot}$, and $\mu_{\rm max}\approx 3300$ for $R_{\rm source}=100\,R_{\odot}$, where a larger $M_{\rm lens}$ yields a greater maximum magnification. The comparison with Table 4 suggests that normal main-sequence stars are unlikely to be observed as microlensing events, and we need to consider either blue supergiants or extremely luminous O-type stars to explain the Warhol event.

As shown in Figure 5, the sources A and B appear to be unresolved in HFF F606W and F814W imaging acquired before the microlensing event. An approximate estimate, assuming a transversal magnification of \sim 100, indicates that the coincident source at positions A and B detected in HFF imaging occurred must be \sim 3 pc at most, so it must be a single star, stellar system, or a compact stellar cluster.

5. Conclusions

In archival HST imaging taken in 2014 September, we have identified a microlensing event dubbed Warhol in a strongly lensed galaxy at z=0.94 very close to the location of the critical curve of the foreground MACS0416 galaxy cluster at z=0.397. The transient's SED is consistent with the presence of a strong Balmer break, expected for blue supergiant stars, which are also the most common very luminous stars at rest-frame optical wavelengths.

The lower temperatures and densities of H-rich stellar eruptions, by contrast, generally lack a strong Balmer jump. Further evidence for a microlensing event is the absence of a second detected transient event near the critical curve, as shown in Figure 4. Time delays should be on the order of days at small separations from the critical curve, yet no corresponding peak at the location of the opposing image is detected in difference imaging. The probability that Warhol could consist of two unresolved images of an outburst is very small, given the comparatively small area in the source plane where any such eruption must occur (Kelly et al. 2018). Warhol's spatial

coincidence with the underlying source in the strongly lensed background implies it is very unlikely to be the explosion or outburst of a star in the intracluster medium.

Furthermore, long-term variation in the light curve measured at Warhol's position is consistent with slow fluctuations expected from microlensing by objects in the MACS0416 intracluster medium. After our paper was submitted, an independent effort to search for highly magnified stars also reported that it had identified Warhol as a candidate (Kaurov et al. 2019). In that work, the research team analyzed the caustic-straddling lensed arc and found evidence for a flux asymmetry across the critical curve. Their analysis detected significant, moderate variability between 2012 and 2014 at Warhol's location, although it did not identify the bright microlensing peak in 2014 September we report here.

The frequency of bright microlensing events including Icarus (Kelly et al. 2018), likely the Spock events (Rodney et al. 2018), and Warhol provide a new probe of the mass density of objects in the intracluster medium (Venumadhav et al. 2017; Diego et al. 2018; Kelly et al. 2018; Oguri et al. 2018), as well as the qualitative properties and luminosity functions of massive stars at high redshift (Kelly et al. 2018). Diego (2019) has found that \sim 50,000 luminous stars at redshifts between z = 1.5 and z = 2.5 should experience an average magnification exceeding 100 from lensing halos of all masses. Of these, approximately 8000 stars should have a mean magnification greater than 250 and should exhibit relatively frequent microlensing peaks. Windhorst et al. (2018) have also recently shown that high magnification during caustic-crossing events close to cluster critical curves should provide an opportunity to observe directly Population III stars at high redshifts using the James Webb Space Telescope. Given that lower magnification microlensing events should be more common than higher magnification events, we expect that our ongoing search of archival HFF cluster imaging may detect additional, fainter events.

This work was supported in part by World Premier International Research Center Initiative (WPI Initiative), MEXT, Japan, and JSPS KAKENHI grants JP15H05892 and JP18K03693. R.J.F. is supported in part by NSF grant AST-1518052, the Gordon & Betty Moore Foundation, the Heising-Simons Foundation, and by a fellowship from the David and Lucile Packard Foundation. Analysis of highly magnified stars at the University of Minnesota by P.L.K is supported in part by NSF grant AST-1908823. P.L.K., A.V.F., and T.T. acknowledge generous financial assistance from NASA/HST grants GO-14922 and GO-14872 from the Space Telescope Science Institute (STScI), which is operated by the Association of Universities for Research in Astronomy, Inc., under NASA contract NAS 5-26555. Additional support for A.V.F. was provided by the Christopher R. Redlich Fund, the TABASGO Foundation, and the Miller Institute for Basic Research in Science (U.C. Berkeley). J.M.D. acknowledges the support of projects AYA2015-64508-P (MINECO/FEDER, UE), funded by the Ministerio de Economia y Competitividad. J.H. was supported by a VILLUM FONDEN Investigator grant (project No. 16599). This work utilizes gravitational lensing models produced by PIs Bradač Natarajan, & Kneib (CATS); Merten & Zitrin; Sharon, Williams, Keeton, Bernstein, and Diego; and the GLAFIC group. This lens modeling was partially funded by the HST Frontier Fields program conducted by STScI. The lens

models were obtained from the Mikulski Archive for Space Telescopes (MAST).

ORCID iDs

```
Patrick L. Kelly https://orcid.org/0000-0003-3142-997X Jose M. Diego https://orcid.org/0000-0001-9065-3926 Masamune Oguri https://orcid.org/0000-0003-3484-399X Adi Zitrin https://orcid.org/0000-0002-0350-4488 Tommaso L. Treu https://orcid.org/0000-0002-8460-0390 Nick Kaiser https://orcid.org/0000-0001-6511-4306 Alexei V. Filippenko https://orcid.org/0000-0003-3460-0103
```

Jens Hjorth https://orcid.org/0000-0002-4571-2306 Jonatan Selsing https://orcid.org/0000-0001-9058-3892

References

```
Akaike, H. 1974, ITAC, 19, 716
Ammons, S. M., Wong, K. C., Zabludoff, A. I., & Keeton, C. R. 2014, ApJ,
   781, 2
Balestra, I., Mercurio, A., Sartoris, B., et al. 2016, ApJS, 224, 33
Bradač, M., Schneider, P., Lombardi, M., & Erben, T. 2005, A&A, 437, 39
Bradač, M., Treu, T., Applegate, D., et al. 2009, ApJ, 706, 1201
Burnham, K. P., Anderson, D. R., & Huyvaert, K. P. 2011, Behavioral Ecology
  and Sociobiology, 65, 23
Caminha, G. B., Grillo, C., Rosati, P., et al. 2017, A&A, 600, A90
Cardelli, J. A., Clayton, G. C., & Mathis, J. S. 1989, ApJ, 345, 245
Castelli, F., & Kurucz, R. L. 2004, arXiv:astro-ph/0405087
Dachs, J. 1970, A&A, 9, 95
Dai, L., Venumadhav, T., Kaurov, A. A., & Miralda-Escud, J. 2018, ApJ, 867, 24
Diego, J. M. 2019, A&A, 625, A84
Diego, J. M., Broadhurst, T., Benitez, N., et al. 2015, MNRAS, 446, 683
Diego, J. M., Kaiser, N., Broadhurst, T., et al. 2018, ApJ, 857, 25
Diego, J. M., Protopapas, P., Sandvik, H. B., & Tegmark, M. 2005a, MNRAS,
Diego, J. M., Sandvik, H. B., Protopapas, P., et al. 2005b, MNRAS, 362, 1247
Diego, J. M., Tegmark, M., Protopapas, P., & Sandvik, H. B. 2007, MNRAS,
   375, 958
Doran, E. I., Crowther, P. A., de Koter, A., et al. 2013, A&A, 558, A134
Ebeling, H., Edge, A. C., & Henry, J. P. 2001, ApJ, 553, 668
Fitzpatrick, E. L., & Garmany, C. D. 1990, ApJ, 363, 119
Flower, P. J. 1996, ApJ, 469, 355
Fruchter, A. S., Hack, W., Dencheva, M., Droettboom, M., & Greenfield, P.
   2010, in Space Telescope Science Institute Calibration Workshop, ed.
   S. Deustua & C. Oliveira (Baltimore, MD: STScI), 382
Gordon, K. D., Clayton, G. C., Misselt, K. A., Landolt, A. U., & Wolff, M. J.
   2003, ApJ, 594, 279
Hoag, A., Huang, K.-H., Treu, T., et al. 2016, ApJ, 831, 182
Jauzac, M., Clément, B., Limousin, M., et al. 2014, MNRAS, 443, 1549
```

```
Jauzac, M., Jullo, E., Kneib, J.-P., et al. 2012, MNRAS, 426, 3369
Johnson, T. L., Sharon, K., Bayliss, M. B., et al. 2014, ApJ, 797, 48
Jones, D. O., Scolnic, D. M., & Rodney, S. A. 2015, PythonPhot: Simple
   DAOPHOT-type photometry in Python, Astrophysics Source Code Library,
   ascl:1501.010
Jullo, E., Kneib, J.-P., Limousin, M., et al. 2007, NJPh, 9, 447
Kaurov, A. A., Dai, L., Venumadhav, T., Miralda-Escudé, J., & Frye, B. 2019,
   ApJ, 880, 58
Kawamata, R., Ishigaki, M., Shimasaku, K., et al. 2018, ApJ, 855, 4
Kawamata, R., Oguri, M., Ishigaki, M., Shimasaku, K., & Ouchi, M. 2016,
   ApJ, 819, 114
Keeton, C. R. 2010, GReGr, 42, 2151
Kelly, P. L., Diego, J. M., Rodney, S., et al. 2018, NatAs, 2, 334
Kim, A., Goobar, A., & Perlmutter, S. 1996, PASP, 108, 190
King, I. 1962, AJ, 67, 471
Liesenborgs, J., De Rijcke, S., & Dejonghe, H. 2006, MNRAS, 367, 1209
Lotz, J. M., Koekemoer, A., Coe, D., et al. 2017, ApJ, 837, 97
McCully, C., Keeton, C. R., Wong, K. C., & Zabludoff, A. I. 2014, MNRAS,
   443, 3631
Merten, J., Cacciato, M., Meneghetti, M., Mignone, C., & Bartelmann, M.
   2009, A&A, 500, 681
Merten, J., Coe, D., Dupke, R., et al. 2011, MNRAS, 417, 333
Miralda-Escude, J. 1991, ApJ, 379, 94
Moffat, A. F. J. 1969, A&A, 3, 455
Oguri, M. 2010, PASJ, 62, 1017
Oguri, M., Diego, J. M., Kaiser, N., Kelly, P. L., & Broadhurst, T. 2018,
   PhRvD, 97, 023518
Oke, J. B., & Gunn, J. E. 1983, ApJ, 266, 713
Patrício, V., Richard, J., Carton, D., et al. 2018, MNRAS, 477, 18
Peng, C. Y., Ho, L. C., Impey, C. D., & Rix, H.-W. 2002, AJ, 124, 266
Pickles, A. J. 1998, PASP, 110, 863
Postman, M., Coe, D., Benítez, N., et al. 2012, ApJS, 199, 25
Przybilla, N., Firnstein, M., Nieva, M. F., Meynet, G., & Maeder, A. 2010,
Richard, J., Jauzac, M., Limousin, M., et al. 2014, MNRAS, 444, 268
Rodney, S. A., Balestra, I., Bradac, M., et al. 2018, NatAs, 2, 324
Sanders, R. L., Shapley, A. E., Kriek, M., et al. 2016, ApJ, 816, 23
Schlafly, E. F., & Finkbeiner, D. P. 2011, ApJ, 737, 103
Schmidt, K. B., Treu, T., Brammer, G. B., et al. 2014, ApJL, 782, L36
Sebesta, K., Williams, L. L. R., Mohammed, I., Saha, P., & Liesenborgs, J.
   2016, MNRAS, 461, 2126
Sérsic, J. L. 1963, BAAA, 6, 41
Smith, N., & Conti, P. S. 2008, ApJ, 679, 1467
Steidel, C. C., Rudie, G. C., Strom, A. L., et al. 2014, ApJ, 795, 165
Stetson, P. B. 1987, PASP, 99, 191
Treu, T., Schmidt, K. B., Brammer, G. B., et al. 2015, ApJ, 812, 114
Urbaneja, M. A., Herrero, A., Bresolin, F., et al. 2005, ApJ, 622, 862
Venumadhav, T., Dai, L., & Miralda-Escudé, J. 2017, ApJ, 850, 49
Watson, W. A., Iliev, I. T., D'Aloisio, A., et al. 2013, MNRAS, 433, 1230
Windhorst, R. A., Timmes, F. X., Wyithe, J. S. B., et al. 2018, ApJS,
   234, 41
Zitrin, A., Broadhurst, T., Umetsu, K., et al. 2009, MNRAS, 396, 1985
Zitrin, A., Meneghetti, M., Umetsu, K., et al. 2013, ApJL, 762, L30
```